UNIVERSITY OF CALIFORNIA OBSERVATORIES

LICK OBSERVATORY TECHNICAL REPORTS

No. 90

ESI, THE NEW KECK OBSERVATORY ECHELLETTE SPECTROGRAPH AND IMAGER

A.I. Sheinis, M. Bolte, H.W. Epps, R.I. Kibrick, J.S. Miller,
M.V. Radovan, B.C. Bigelow, B.M. Sutin

Santa Cruz, California
January, 2002

ABSTRACT

The Echellette Spectrograph and Imager (ESI) is a multipurpose instrument which has been delivered by the Instrument Development Laboratory of Lick Observatory for use at the Cassegrain focus of the Keck II telescope. ESI saw first light on August 29, 1999. The optical performance of the instrument has been measured using artificial calibration sources. Measurements of the average image FWHM in echellette mode are 22 microns (0.″22) and they are comparable in the low-dispersion and direct-imaging modes . ESI contains a unique flexure compensation system that reduces the small instrument flexure to negligible proportions. Images on the sky show FWHM of 34 microns (0.″34) averaged over the entire field of view. These are the best non-AO images taken in the visible at Keck Observatory to date. Maximum efficiencies are measured to be 30% for the echellette mode and greater than 40% for low-dispersion prismatic mode including atmospheric, telescope and detector losses. In this paper we describe in detail the instrument and its development. We also discuss the performance-testing and some observational results.

Subject headings: esi, instrumentation: spectrographs, imager, echellette, Keck, instrumentation, spectroscopy, astronomy

Contents

1. Overview

The Echellette Spectrograph and Imager (ESI) is a recently commissioned instrument available for use at the Keck II telescope of the W.M. Keck Observatory. ESI was built at

the Instrument Development Laboratory of UCO/Lick Observatory at the University of California, Santa Cruz campus. ESI instrument has three modes. The 160-mm collimated beam can be sent directly into the camera for direct imaging, through a prism disperser for low resolution spectroscopy, or to an echellette grating with prism cross-dispersion for moderate-resolution, large-wavelength-coverage spectroscopy.

An all-refracting ten-element camera and a single ($2K \times 4K by 15$-micron) CCD detector are used without modification for all three modes. The direct-imaging mode has a ($2.0' \times 8.0'$) field of view (f.o.v.) with $0''.15$ pixels. The low-dispersion prism-only mode (LDP) has a reciprocal dispersion of 50 to 300 km/sec/pixel, depending on wavelength. This mode can be used with an $8'.0$-long slit or in a multi-slit mode with user-made slitmasks. The high-dispersion echellette mode gives the entire spectrum from 0.39 to 1.09 microns with a $20''.0$ slit length in a single exposure. The reciprocal dispersion in echellette mode varies from 9.6 km/sec/pixel in the bluest order to 12.8 km/sec/pixel in the reddest order. Three five-bay filter wheels provide locations for up to eight different full-field filters, three multi-object slit masks and the standard complement of five echellette slits in a single bay. Each wheel also contains a single open bay.

The instrument was delivered to Keck II in July of 1999 and saw first light on August 29, 1999. In its first two years of operation it has been scheduled for an average of 111 nights per year and it has proven to be reliable, efficient with photons and efficient with observing time. In the imaging mode, ESI routinely delivers remarkable image quality. Long exposures with FWHM values $< 0''.45$ have been commonly obtained.

The Principal Investigator (PI) of the project was Joe Miller, Director of Lick Observatory. ESI also had three Co-PI's; Michael Bolte, Puragra Guhathakurta, and Dennis Zaritsky. The optical designers were Brian Sutin and Harland Epps. David Cowley was the project manager. Initially (11/95 - 7/97), Bruce Bigelow was the project scientist.

After Bigelow left for Carnegie Observatory and for the remainder of the project, the project scientist responsibilities were split between project engineers Matt Radovan and Andrew Sheinis.

The principal niche envisioned for ESI was very high-throughput moderate-resolution optical spectroscopy with wide wavelength coverage in a single exposure. Examples of the science programs which drove the choice of resolution are kinematic and abundance studies of distance galaxies, detailed abundance determinations for stars as faint as V= 22 (which includes the bright giants in Local Group galaxies) and absorption-line studies in the line-of-sight to QSOs. The low-dispersion/multi-object and direct-imaging capabilities were added after the echellette design was conceptualized. In the low-dispersion mode, ESI is likely the most powerful spectrograph in operation for obtaining low-resolution spectra of extremely faint objects. Redshift determinations and spectral energy distribution measurements for very faint galaxies or low-luminosity stars in the Galaxy are possible to V$\approx$ 25. Examples of first-light science can be seen in Becker et al. (2000) and Prochaska et al. (2001).

This paper serves as a comprehensive overview of the instrument. For details about the individual subsystems, the reader is directed to the other articles in the literature describing various aspects of esi; Kibrick et al. (2000a), Sheinis et al. (1999a), Sheinis et al. (1999b), Radovan et al. (1998), Sheinis et al. (1998), Epps (1998), Epps & Miller (1998), Sutin (1997), Bigelow & Nelson (1998), Sheinis et al. (2000). For observers planning to use esi, the Keck Observatory WWW site for the instrument http://www2.keck.hawaii.edu:3636/realpublic/inst/esi/esi.html contains detailed specifications and descriptions of operation procedures.

The wavelength range of ESI was chosen to lie between 0.39 microns where the best glasses for the visual range become acceptably transparent, up to 1.1 microns where the

efficiency of silicon CCD detectors aproaches zero. The f.o.v. imaged by ESI is a rectangle located 5.′0 off-axis from the telescope axis, and it is 2.′0 wide in the axial direction by 8.′0 long. With this f.o.v., an on-axis (nearly) parabolic collimator, imaging an off-axis field was required to minimize off-axis aberrations. The focal length of the collimator was chosen to be the longest that would fit into the Cassegrain module envelope, giving a 160.0-mm beam. After the collimator, the optical elements used in the instrument are: two flat fold mirrors; two prisms; a grating; the camera and shutter assembly; and the Dewar.

The requirements for the spectrograph layout are:

- The echellette spectral format must fill the CCD chip efficiently;
- The orders must not overlap when a 20.″0 slit is used;
- The individual slit images must be quasi-parallel over the entire detector;
- The incoming beams should have minimum vignetting at the camera mouth.

Mode 1: Echellette in near-Littrow configuration

The primary mode of the spectrograph uses a catalogue echellette grating, operating in 10 orders, from order-6 in the red to order-15 in the blue. Table 1 shows diffraction orders, wavelength ranges and reciprocal dispersions for the echellette mode. The general specifications for this mode are listed below:

- Average Resolution: 11.4 km/sec/pixel average, 9.8 to 12.7 km/sec/pixel range;
- Spectral Resolution: At minimum slit width = 2 pixels = 0.″3, R = 13,000;
- Spectral coverage: 0.39 to 1.1 microns with no gaps in a single exposure;

Table 1: Predicted Performance, Echelle Mode

ORDER	range(μ)	$D_{rms}(\mu)$	D_{rms}(arcseconds)	Å/pix	arcseconds/pix
15	$0.393 \cdots 0.419$	12.01	0.122502	0.15	0.127
14	$0.420 \cdots 0.451$	16.03	0.163506		0.133
13	$0.451 \cdots 0.486$	19.58	0.199716	0.18	0.141
12	$0.487 \cdots 0.529$	19.15	0.19533	0.19	0.148
11	$0.529 \cdots 0.581$	17.2	0.17544	0.21	0.153
10	$0.581 \cdots 0.640$	17.86	0.182172	0.23	0.159
9	$0.640 \cdots 0.715$	22.24	0.226848	0.26	0.164
8	$0.715 \cdots 0.813$	25.46	0.259692	0.29	0.171
7	$0.813 \cdots 0.937$	24.19	0.246738	0.33	0.177
6	$0.937 \cdots 1.093$	15.93	0.162486	0.39	0.183

- Pixel size on the sky: 0.″153 in reciprocal-dispersion direction, 0.″127 - 0.″183 in slit direction (due to prism anamorphic distortion);
- Echellette dispersing element is a single grating in fixed position (Spectronics 204 × 204 mm, 175 lines/mm, 32.3 degrees blaze angle;
- Cross dispersion is provided by two Ohara BSL7Y prisms, one used in double pass (pre-dispersion);
- Order spacing is 22.″0 minimum for the echellette orders 6 - 15.

Figure 1 shows the physical layout of the spectrograph in echellette mode. The collimated light from a 20.″0 slit is pre-cross-dispersed by the first prism before hitting the grating. The echellette grating is used nearly in Littrow for high efficiency. Although the spectrograph was designed specifically for this grating, other gratings could be manually installed. The grating-dispersed light is once again cross-dispersed by a second pass through the aformentioned prism. It then passes through the second prism before being imaged onto the detector by the f/1.07 camera (which operates effectively at about f/1.9).

Figure 2 shows a raw echellette spectrum of a reference star. The entire spectral range from 0.39 to 1.09 microns is imaged without gaps. Orders run from 6 at the top to 15 at the bottom with red to the right. Note the two chip defects which are a partial hot row in the lower right and the hot pixel, also in the lower right. While these defects add some complexity to the data reduction, they do not reduce the spectral coverage of the instrument as they are both located in wavelength overlap regions.

Figure 3 shows the calculated residual tilt of the slit images as a function of wavelength. Orders are curved primarily by the anamorphic distortion in the prisms, but they show a reasonably constant wavelength solution as a function of slit height. Hence we see very little variation in the slit tilt with wavelength.

Figure 4 shows the calculated RMS image diameters as a function of wavelength for all of the echellette orders. The plot includes aberrations from the entire optical train. The diameters were calculated by apodizing the irregularly-shaped Keck II primary mirror and by assuming perfect seeing. The 90-percent encircled energy diameters are not shown but their plot is similar, with an average diameter of 30.0 microns, or two pixels, rather than 20.0 microns.

Figure 5 shows the reciprocal dispersion as a function of wavelength for each order in the echellette mode. The average reciprocal dispersion is about 11.4 km/sec/pixel.

Mode 2: High-efficiency, low-dispersion configuration

The high-efficiency mode bypasses the grating by inserting a flat mirror in front of the echellette grating and rotating the slit direction 90 degrees. The general specifications for this mode are:

- Reciprocal dispersion: variable, from 60 to 350 km/sec/pixel;
- Spectral coverage: 3900-11000 Å in a single exposure;
- Throughput: up to 42 % including detector (for "fresh" telescope coatings);
- Multi-slit mode: 10 - 50 objects using slit masks.

Figure 6 shows the physical layout in this mode. Since the exit pupil of the collimator is near the prisms, the field of view in this mode is not significantly restricted by vignetting at the prisms, so a long slit may be used. The 8.0-arcmin maximum slit length is where the images begin to get "soft". With a field this long, up to 50 slitlets could be cut into a slit mask within the $2\farcm0 \times 8\farcm0$ viewing area. The main strength of this mode is the high throughput as the aluminized grating has been replaced by a higher-efficiency silvered mirror.

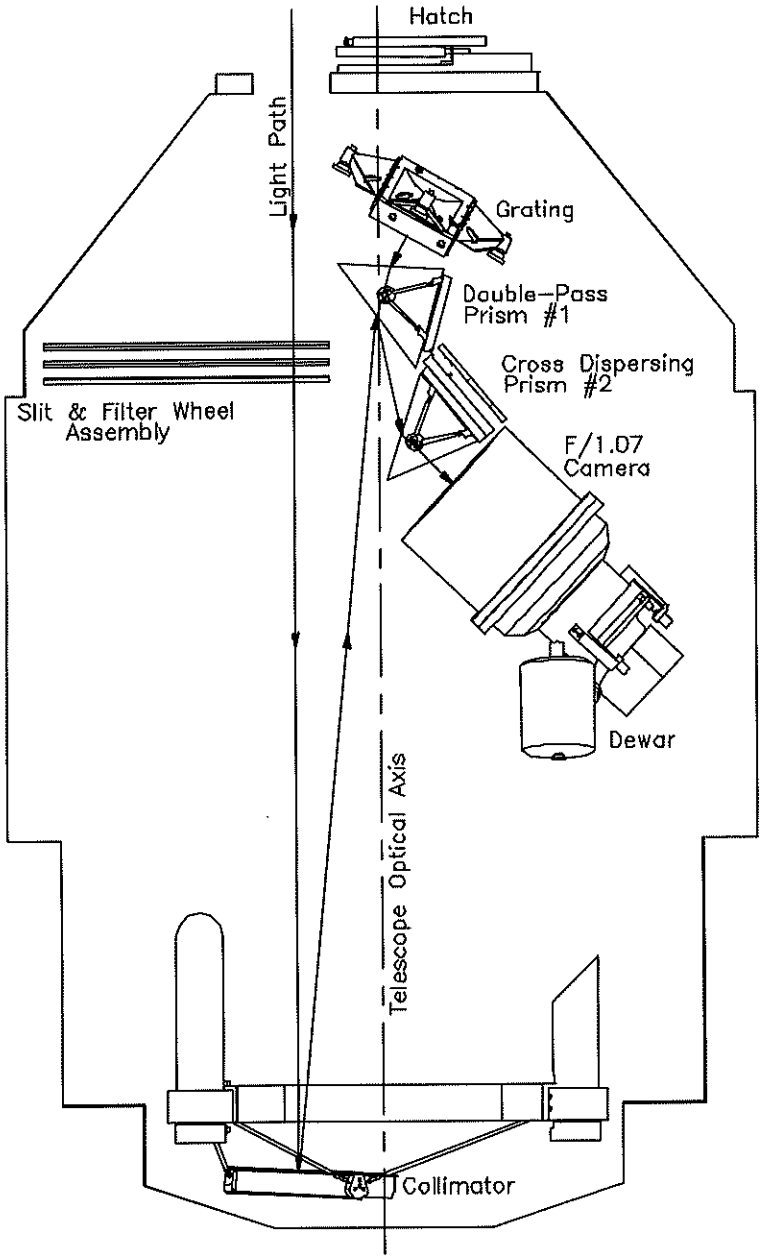

Fig. 1.— Schematic layout of Echellette mode.

Figure 7 shows the spectrum of a reference star taken in this mode with esi. This image has been processed using the Information data language (IDL) so as to align the apparent dispersion direction approximately with a single row. Note the curved sky lines due to the prisms anamorphic distortion.

Mode 3: Direct imaging configuration

The direct imaging mode bypasses the grating and the prisms by inserting a flat mirror ahead of the pre-disperser prism, and by retracting the second prism from the optical path. The general specifications for this mode are:

- Field size: rectangular, $2\farcm0 \times 8\farcm0$ f.o.v.
- Pixel size on the sky: $0\farcs153$
- Standard filters , ($2\farcm0 \times 8\farcm0$ each) Johnson (B), Johnson (V), Spinrad (R), Gunn (I).

Figure 8 shows the physical layout of this mode. The filter wheel near the telescope focal surface is required for narrow-band interference filters, which cannot be in the parallel beam without causing passband dependence upon field angle. The image sizes are uniform over most of the f.o.v., a feature which is also true in the low-dispersion prism-only spectroscopic mode.

Figure 9 shows a pseudo-color image of planetary nebula NGC 7009 taken in B,V,R, and I filters.

2. Opto-Mechanical Subsystems

The design of ESI was divided into several natural subsystems, namely: The collimator; the prisms; the opticals flats including the grating; the camera assembly; the detector

and controller; the slit and filter wheel assembly; the calibration system; and the guider assembly. We now describe each of those subsystems in detail.

2.1. Collimator

The collimator mirror is 0.58 m in diameter to accommodate the $2\farcm0 \times 8\farcm0$ f.o.v.. It has a focal length of 2.286 m. The range of focus was selected to be ± 25 mm which gives out-of-focus star-image diameters of $2\farcs4$. The collimator mirror is optimally constrained by a space-frame structure. It is actively articulated in piston, tip and tilt to provide the focus and the flexure control for the instrument. The flexure compensation is accomplished by applying calibrated active correction for gravity flexure in an open-loop fashion.

2.1.1. Requirements

The requirement for any two-hour observation was that the spectra should remain stable on the detector to within $\pm 0\farcs04$ (peak-to-valley) with (open-loop) flexure compensation. At the final imaging scale of $0\farcs153$ per pixel, this requirement corresponds to $\pm\frac{1}{4}$ pixel. In order to achieve the required flexure compensation precision, collimator tilt increments must be controlled in $0\farcs01$ units upon the sky, corresponding to collimator tilts of $0\farcs327$. With actuator separations of 1200 mm, that corresponds to actuator motions of 1.65 μ. In order to achieve the desired correction precision, hysteresis and slip levels were maintained below this value.

2.1.2. System Design

The collimator system design is pictured in Figure 10. The support solution for the collimator consists of three Invar pads which were glued to the outer girdle of the mirror. The locations for these pads were optimised to reduce the collimators overall surface deformation. These pads are attached to a six-strutted hexapod structure. The structure was designed such that each of the struts carries loads in tension or compression only. The structure is determinate because it uses six struts to constrain six degrees of freedom. Any motion of a strut endpoint (node) or any change in strut length only causes free-body motion of the collimator without internal stress. In this way, the design isolates the collimator from residual stresses in the main-frame structure.

We modelled the final design. The result was a peak-to-valley surface deformation of 0.25 μ over the active area of the collimator. This occurs when the telescope is pointed near the zenith. Since the area on the collimator illuminated by any individual star is only 160 mm in diameter, the surface deformations cause two different aberrations. The RMS slope variation averaged over any 160 mm diameter results in an image quality degradation of less than 0.″012. The mean slope error with respect to the surrounding field causes a maximum image motion of about 0.″01 (differential field distortion).

The ESI collimator design includes a safety system composed of two thin plates attached to each of the Invar pads. This safety system supports the mirror in the unlikely event that an epoxy joint should fail. It is designed such that it does not support or constrain the mirror mount in normal operation.

The collimator support structure is attached to the spectrograph main-frame with three linear actuators. These actuators provide the collimator with the piston, tip and tilt articulation which is required to control focus and flexure. They are designed as three independent cartridge assemblies which mount in the lower tubes of the main-frame. Each

assembly is mounted to the inside of the tube with six push-pull screws in order to allow alignment of the actuators with the optical axis of the instrument. A complete cartridge assembly is composed of a THK High Precision (6-mm lead) ball-screw slide, driven by a Galil (4000 count/revolution) servo-motor encoder through a 100:1 gearbox. A 1/10-micron Renishaw linear encoder is included in each assembly. This encoder provides the feedback for the dual-servo control loop. Each assembly also includes primary as well as secondary limit switches and mechanical hard stops. Due to the large reduction through the gearbox and the lead screw, each Renishaw encoder count is equal to six motor encoder counts. This servo-system delivers repeatable positioning to $0\farcs04$ of collimator tilt over the entire $\pm$25-mm range of focus.

2.1.3. Analysis and Testing

The first natural frequency of the collimator support was measured to be 75 Hz. This corresponds to a maximum gravity driven-deflection of XXX Hz.

Repeatability testing showed that each actuator could be moved to any desired position within two Renishaw counts, which corresponds to a maximum tilt error of $0\farcs04$ as mentioned above. When two of the actuators were slaved to a third for focus motion, the total error increased to three encoder counts ($0\farcs06$ tilt). Bench tests of the THK actuators resulted in a measurement of 1 micron of hysteresis which is marginally adequate to meet the system specification.

Additionally, the collimator support system was tested by applying 300-Newton loads orthogonally in three directions. We were unable to measure any hysteresis larger than our $1\farcs0$ measurement-resolution limit for this test. This limit was marginally appropriate to the task.

2.2. Cross-Dispersion Prisms

2.2.1. Optical Requirements

ESI uses two large (25 kg), 50.0°-angle prisms for cross-dispersion. The optical requirements for the prisms were high transmission, small index inhomogeneity, a large ratio of red dispersion relative to blue dispersion while maintaining as high an index as possible. Fused silica was considered, however its relatively low index would have required 55.0°-prisms which would have complicated the optical and coating designs. Ohara BSL7Y was selected for the prisms as it's optical properties provide an optimal combination of the requirements listed above.

Various index-inhomogeneity models for the prisms were computed and ray traced. The results of this modeling suggested that the index homogeneity must be constant to approximately $\pm 10^{-5}$. Our contract with the vendor did not guarantee this level of precision. However interferograms of the finished prisms taken in transmission, along with the final image quality tests, show that the fabricated prisms are homogeneous to approximately $\pm 2 \times 10^{-6}$.

2.2.2. Prism Mounting

The prisms are mounted within the spectrograph using determinate structures. These structures are extremely rigid for their weight because mount material is used in compression or tension only. The mounts are designed such that no moments can be imparted at the mount-to-glass interfaces, thereby insuring that the glass is isolated from any mechanical stresses developed inside the instrument structure.

2.2.3. Design Requirements

The cross-dispersion prisms are illuminated in collimated light. Their most important stability criteria are control of tip and tilt, with little requirement for displacement control. The sensitivities for the double-pass prism are $\pm 0\farcs013$, $\pm\ 0\farcs005$, and $\pm\ 0\farcs014$ of image motion in echellette mode for $\pm\ 1\farcs0$ of prism tilt about the local X, Y, and Z axes respectively. Z is the local optical axis, X is in the plane of the prismatic dispersion and Y is perpendiclar to the plane of prismatic dispersion. The required spectrograph performance is $\pm\ 0\farcs04$ of image motion with (open-loop) flexure control for any two-hour integration. For a reasonable choice of the allowable percentage of the total error allotted to the prism motion, these sensitivities give a requirement of less than $\pm\ 1\farcs0$, $\pm\ 2\farcs0$ and $\pm\ 1\farcs0$ of tilt about the X, Y and Z axes, respectively.

Several other important requirements for the mount design are; 1) minimization of measurable hysteresis, 2) the ability to make a one-time alignment adjustment of the prism tilts over a $30\farcm0$ range during the initial assembly, 3) removability of the prisms for re-coating, with a repeatable alignment position upon re-assembly. Additional desirable design features for the prism mount system include a handling fixture, light baffling and a mechanism to retain the prism in the unlikely event of glue failure.

The normal operating temperature range for Keck instruments is $2\fdg0 \pm 4\fdg0$ C and the survival range seen at the summit is $-15\fdg0$ to $20\fdg0$ C. We designed the prism mounts to be athermal with respect to tilts over the operating temperature range. Moreover, the mounts were designed to isolate the prisms from thermally-induced stresses over a range greater than the survival temperature range.

2.2.4. Design Details

The final design for is pictured in Figures 11 and 12. A six-strutted, determinate structure is mounted to each prism via tantalum pads bonded to each of the three unilluminated prism faces . Tantalum was chosen as the pad material to minimise thermally-induced stresses in the glass because the thermal expansion coefficient of tantalum closely matches that of the BSL7Y prisms. The structure for the single-pass prism is bolted to a translation stage on the Optical Sub-Structure (OSS) in four locations. Initial adjustment was accomplished by shimming the bolted connection points.

In order to minimize rotation, the pad locations on the prisms and connection points on the OSS were optimised via a finite element analysis (FEA) model and via detailed testing with a physical model. The final rotations due to gravity as determined by the FEA are shown in Table 2. The physical model was a complete prism-mount system, using substitute prisms fabricated from aluminum and concrete to match the mass, volume and shape of the real prisms. A rotating platform was used to simulate the varying orientation of gravity with respect to the spectrograph. Translation and rotation of the physical model were measured using capacitive contact probes.

Each strut in the prism mounting contains a pair of "flexure mechanisms" to allow rotation at the connection points while maintaining overall length dimensions. Flexure thicknesses and lengths were designed to impart less stress than the self-weight loading of the prism imparts into the prism pad connections. The flexures were also designed to keep the induced stress below the elastic limit over the full range of adjustment, while keeping the strut as stiff as possible. Strut thickness calculations and FEA are described by Sheinis (1999). Pad areas were chosen to give a self-weight induced stress of 125 KPa. This provides a safety factor of 50. Glue thickness and type was chosen based on the work of Iraninejad et al., (1987) related to the glue connections for the Keck primary mirrors.

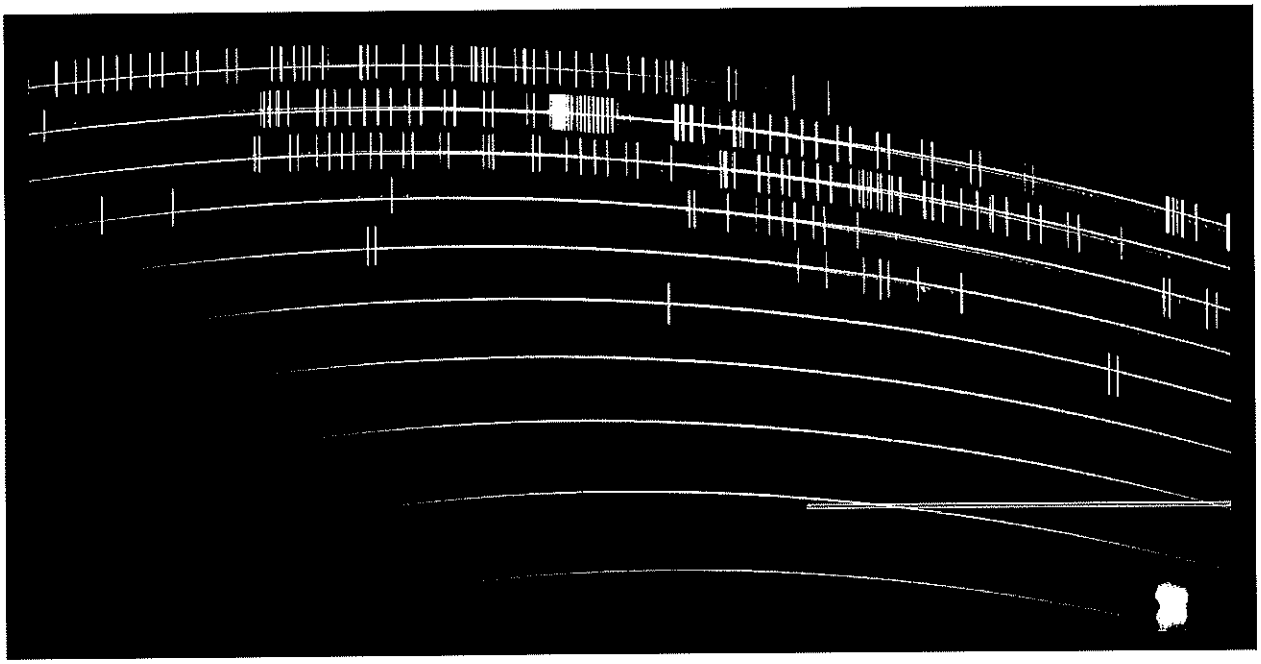

Fig. 2.— Echellette spectrum.

Table 2: Gravity induced rotation

Gravity direction	Rotation about X (arcseconds)	Rotation about Y (arcseconds)	Rotation about Z (arcseconds)
X	0	0.59	0
Y	0.56	0	0
Z	0	0.15	0.19

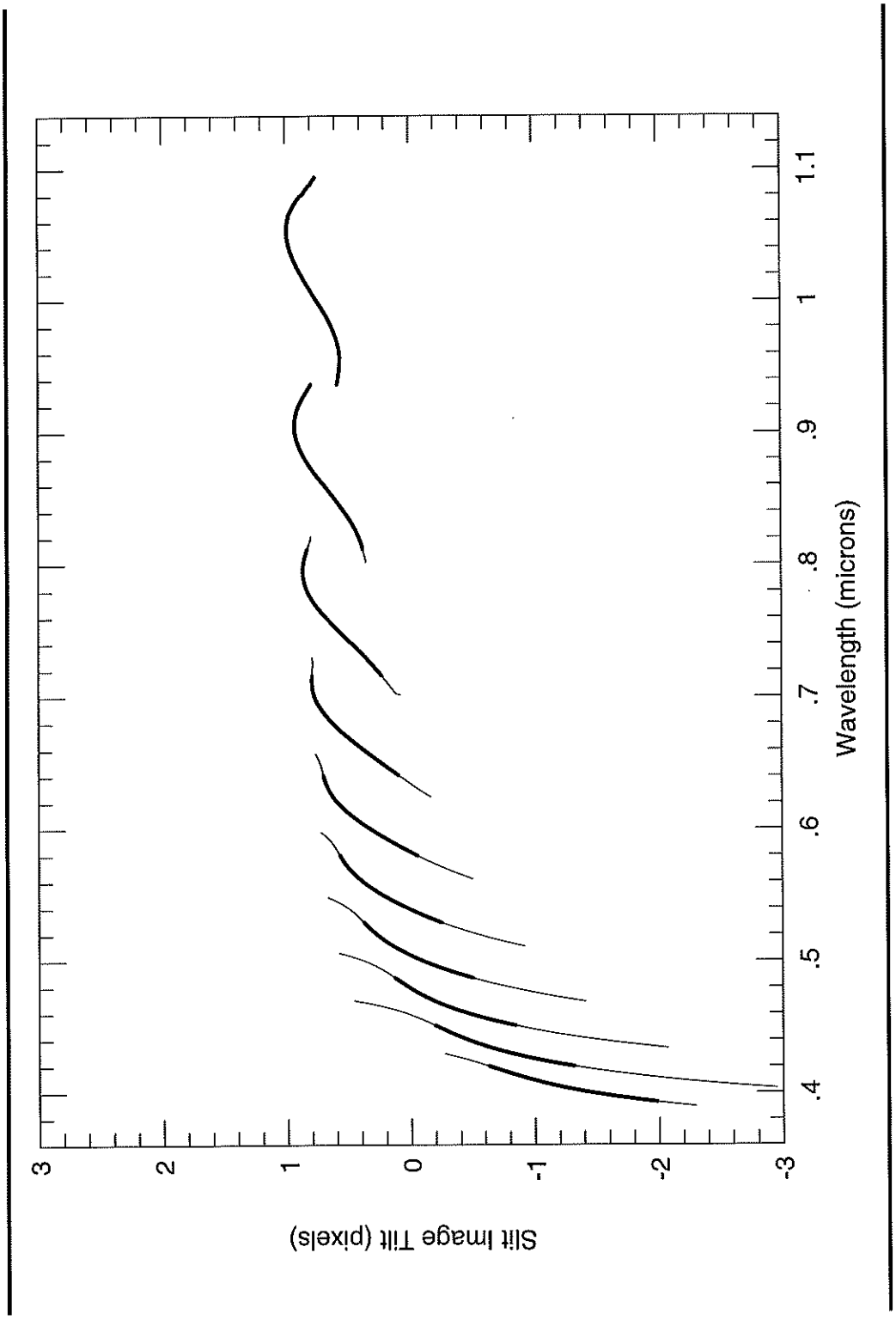

Fig. 3.— Tilt of slit images in echellette mode.

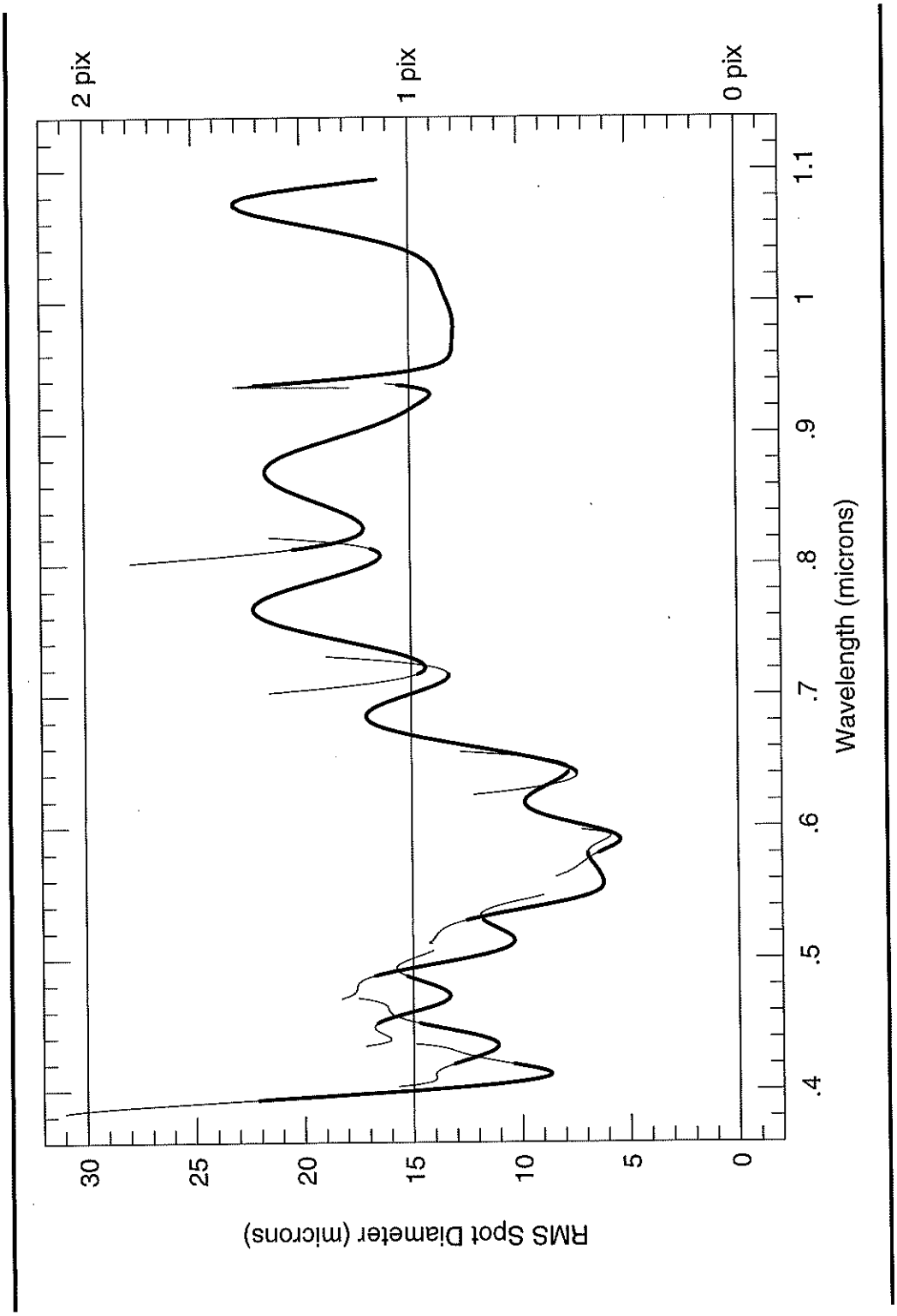

Fig. 4.— Spot size in echellette mode.

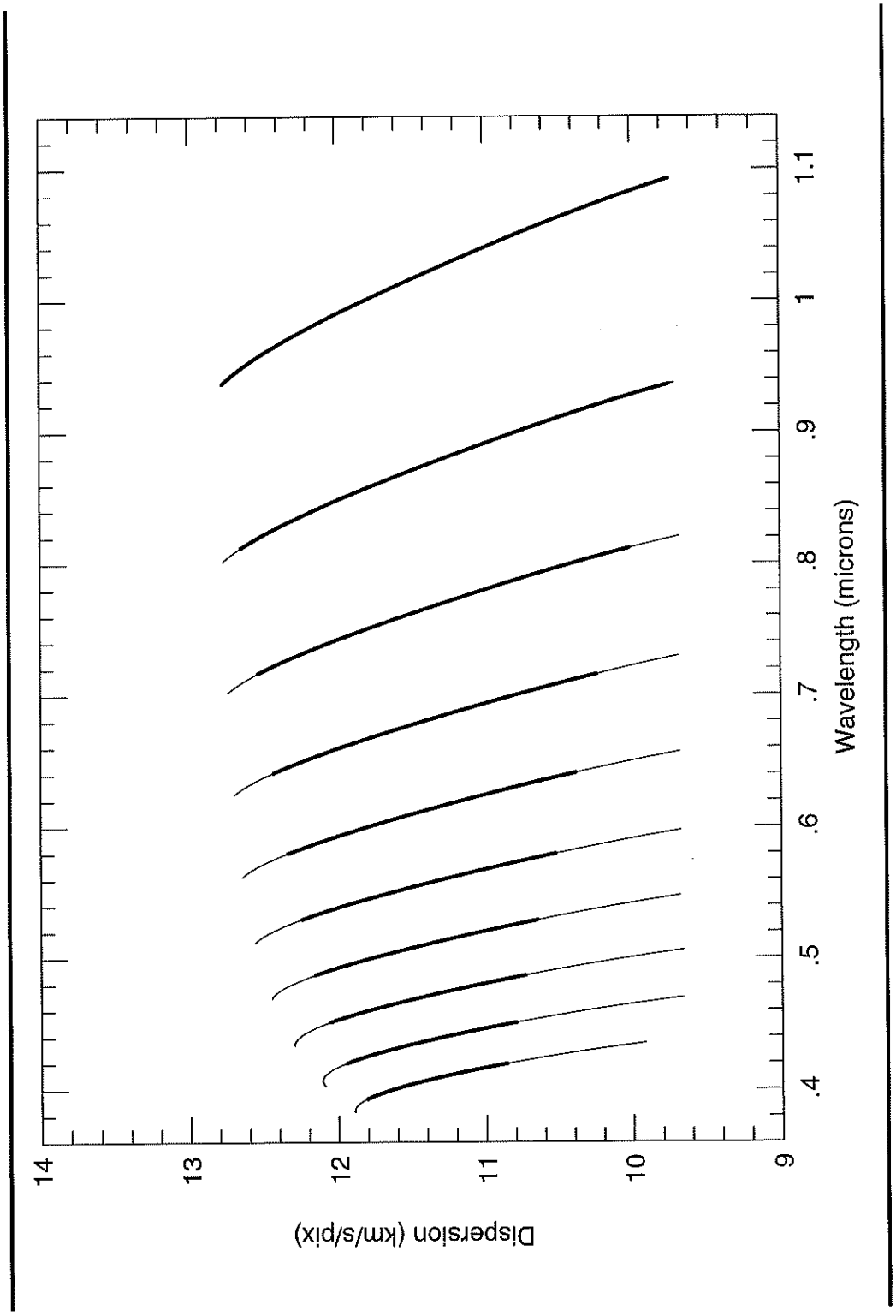

Fig. 5.— reciprocal dispersion in echellette mode.

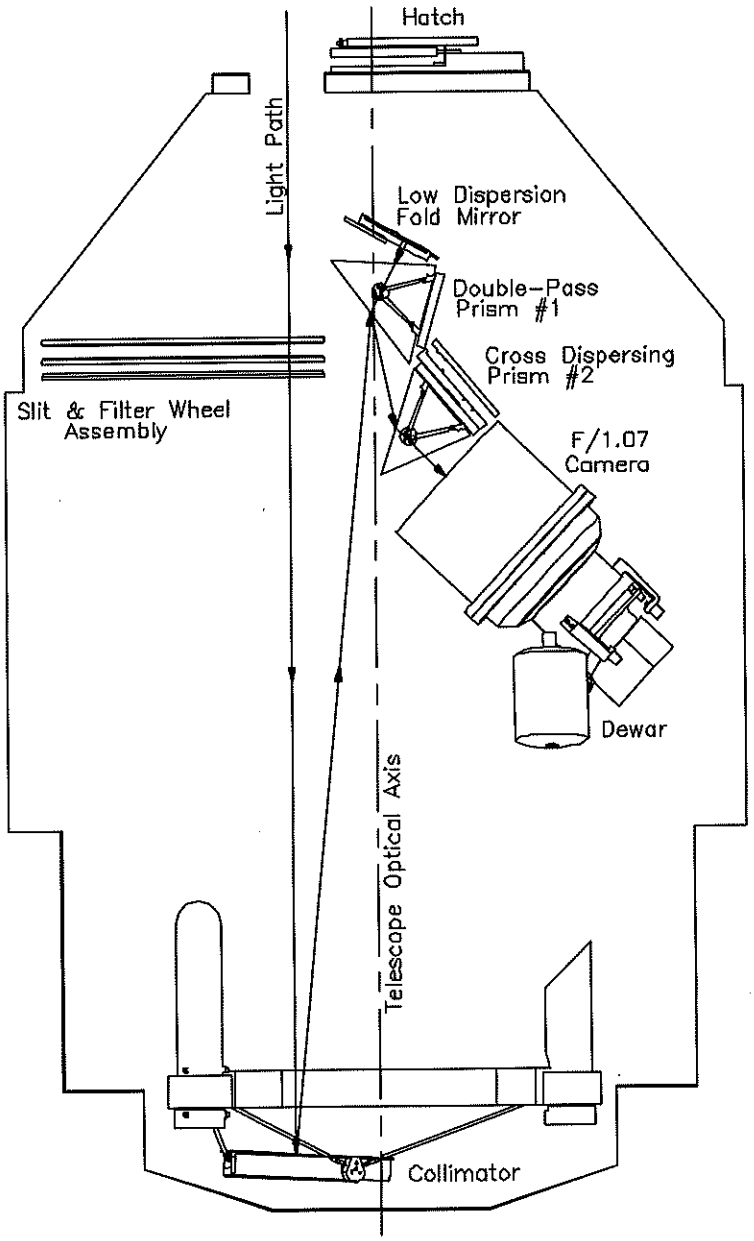

Fig. 6.— Schematic layout of Prismatic mode.

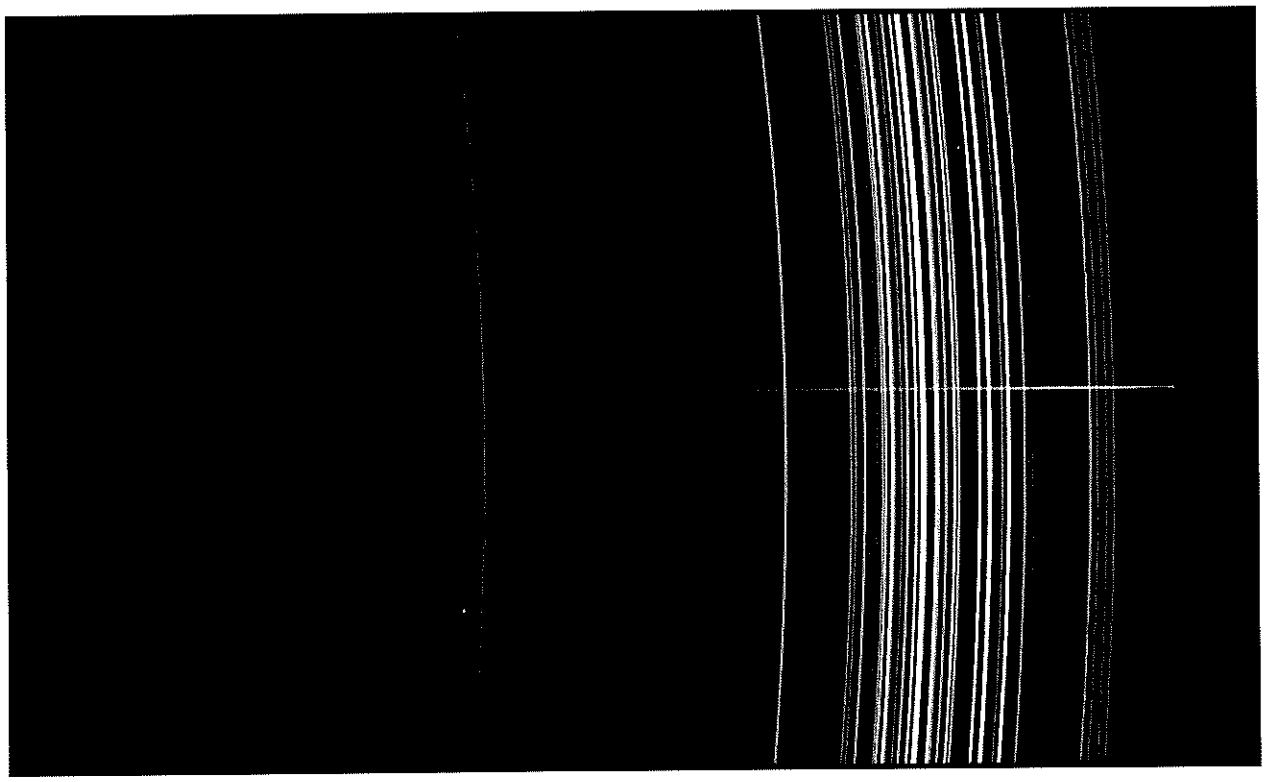

Fig. 7.— Prismatic mode spectrum.

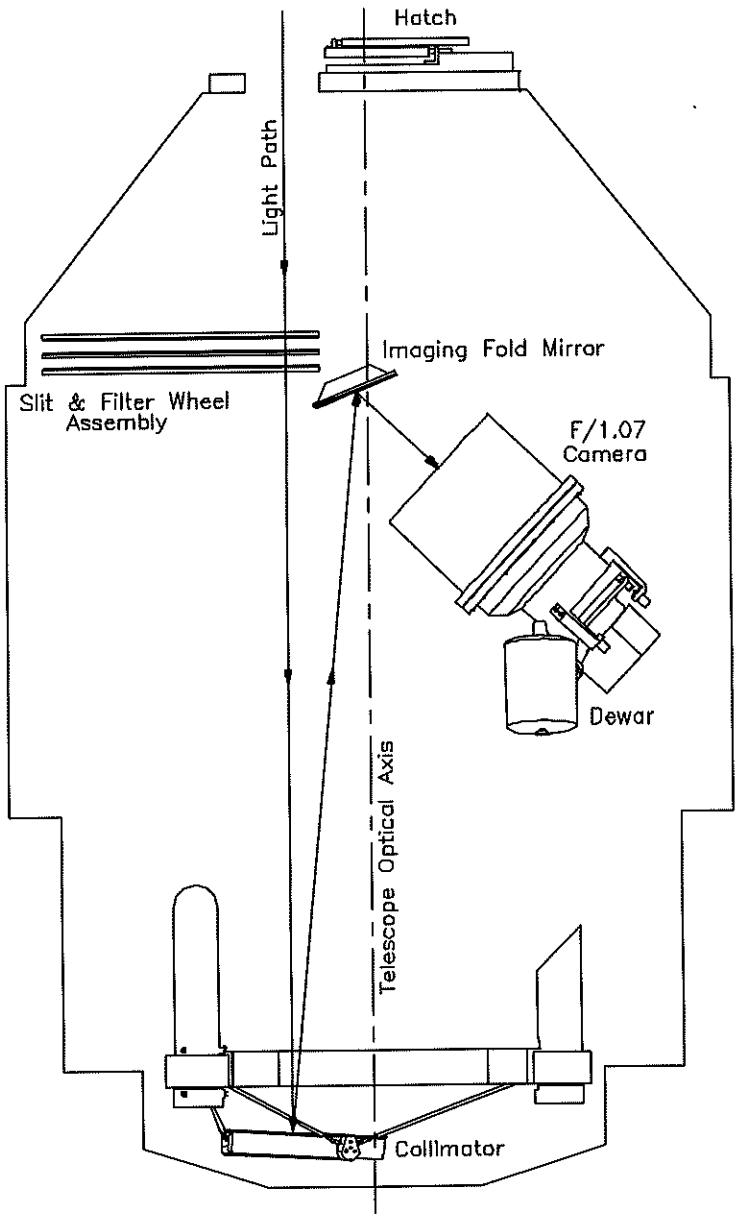

Fig. 8.— Schematic layout of direct imaging mode.

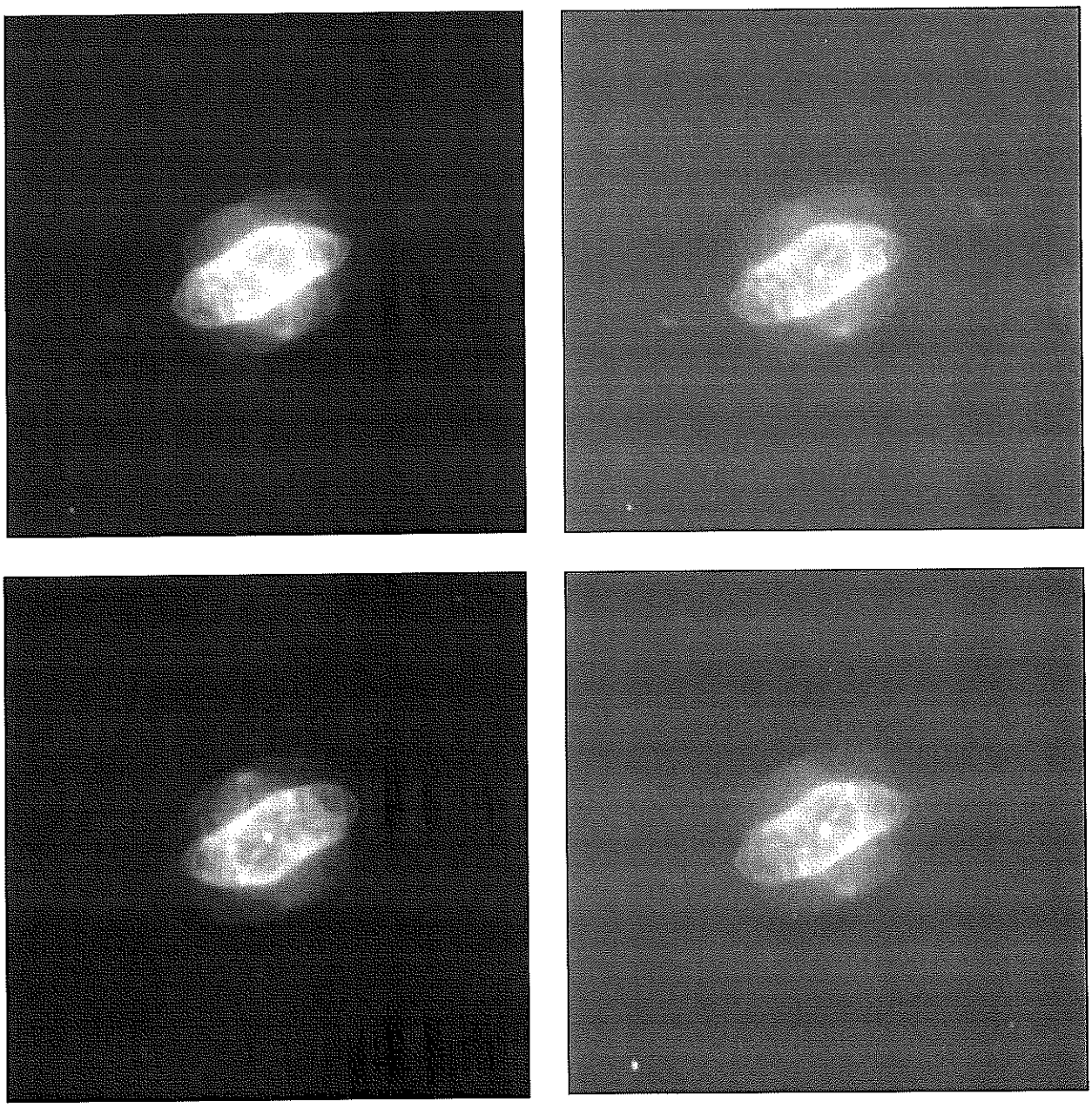

Fig. 9.— NGC 7009 in B,V,R,I .

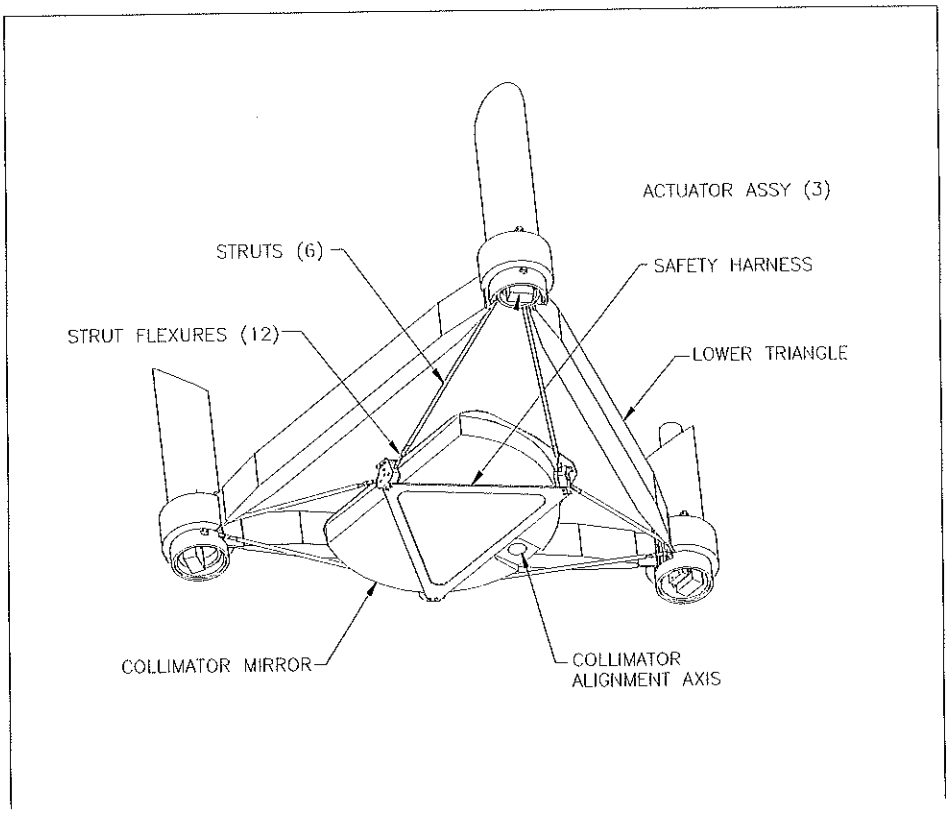

Fig. 10.— **E**SI Collimator system.

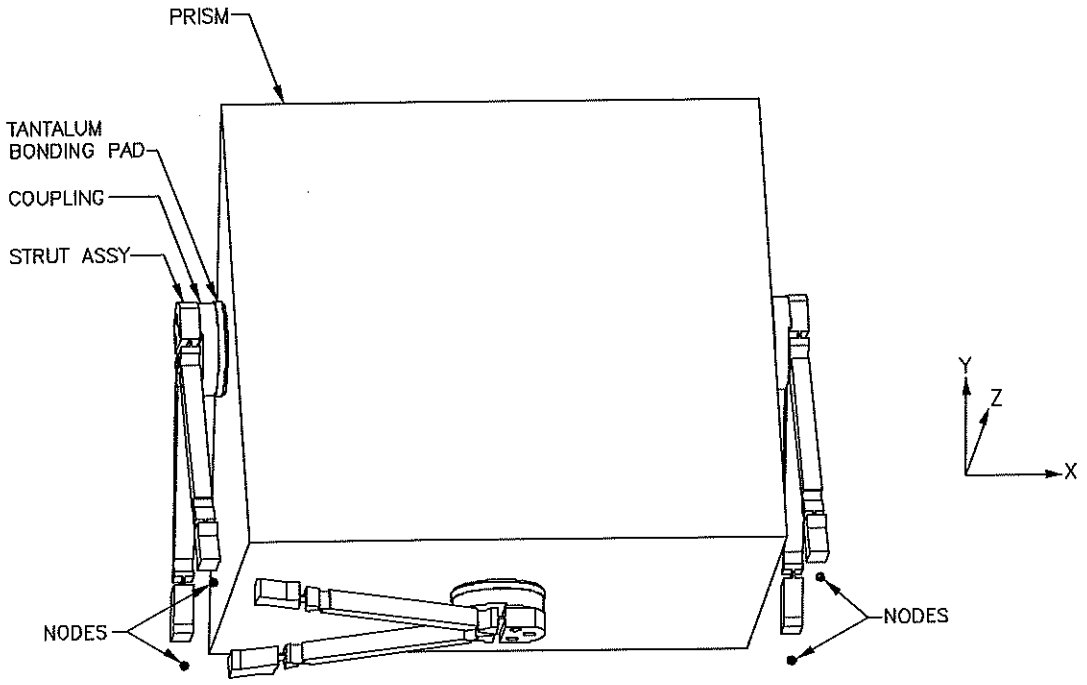

Fig. 11.— Prism mount geometry.

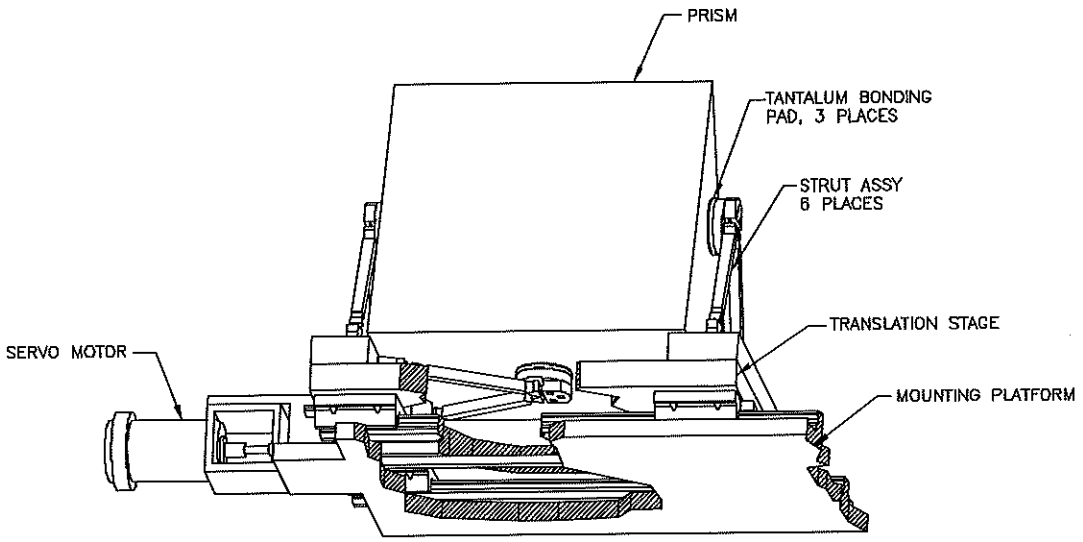

Fig. 12.— Prism locator assembly.

2.3. Kinematic mirror mechanisms

ESI uses two moderate weight (10kg) translating fold mirrors to switch between modes. These must locate in angle and position accurately. A novel locating mechanism design was developed to achieve the repeatability needed for these mirrors. In the following section, we will detail this design using the imaging-mode fold mirror (IM) as an example. The mount for low-dispersion-mode fold mirror (LDM) is designed in a similar manner .

2.3.1. Requirements

The scientific requirements for the spectrograph are such that the spectra may move by no more than $\pm 0\farcs04$ on the sky ($\frac{1}{4}$ pixel) in switching between modes so as to accomodate the use of a single set of standard reference spectra and flat-field data between different exposures. This places a $\pm 1\farcs3$ allowable tip and tilt repeatability on the LDM. A similar requirement was adopted for the IM. The packaging constraints left little space for a conventional translation stage for either mirror. Given these requirements and constraints, we determined that a conventional translation stage could not be used.

2.3.2. Opto-Mechanical Design

The mechanical system design for this translation system is pictured in Figures 13, 14, and 15. The six degrees of freedom of the IM are constrained by three V-blocks containing six kinematic locating surfaces rigidly mounted to the OSS and three tooling-ball assemblies bonded to the mirror via Invar pads. The mirror is positively located by translating it in such a way that the three tooling balls contact all six locating surfaces. The requirement is to get the tooling balls to locate in the V-blocks (which can require a considerable amount of force), while minimizing the amount of residual stress within the mirror.

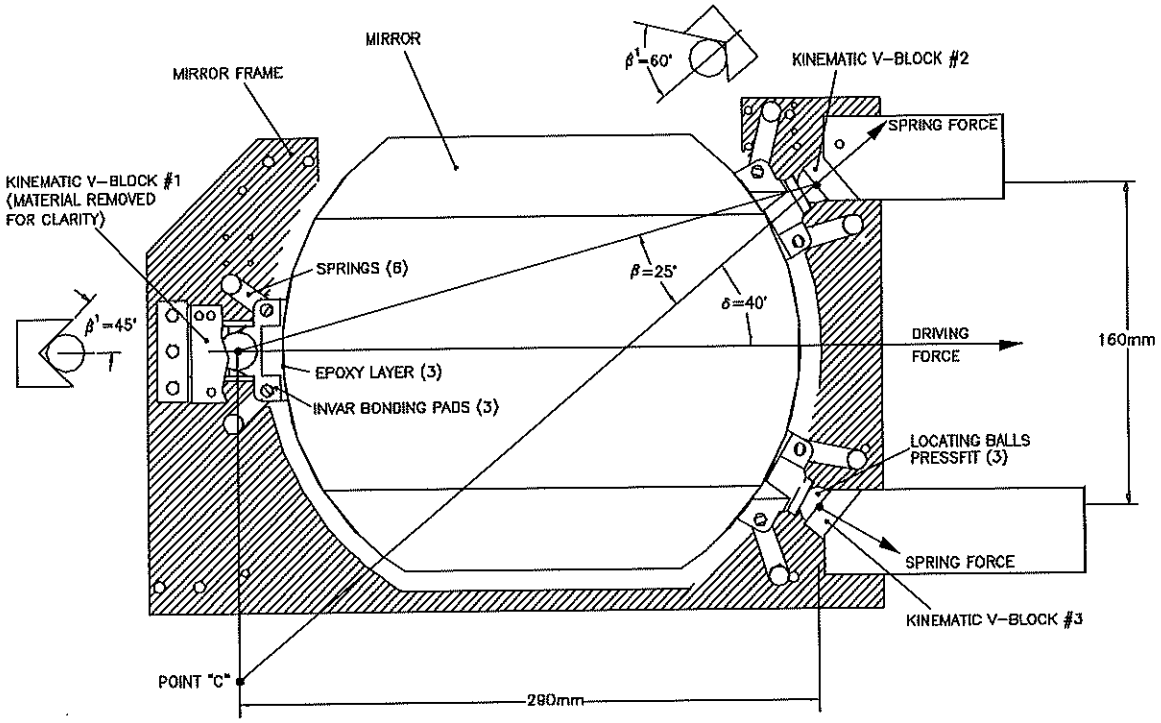

Fig. 13.— Mirror locator, details.

We met this requirement by mounting the mirror with springs attached to the aforementioned Invar pads and to a frame. The frame serves as a translating carrier for the mirror. When the frame is driven toward the mirror-active position, the tooling balls approach the V-blocks and the frame moves forward until all six V-block surfaces are contacted. After contact is completed, the forward four springs elongate, increasing the force on the balls. Simulatneously the rear two springs contract, reducing the amount of force passing through the glass. In this way, the full-tension force can be applied to the kinematic loading points, while having near-zero stress transmitted through the glass (neglecting friction).

We were able to cantilever the frame on very small crossed-roller slides because the lateral position tolerance on the frame is loose. In the direction of motion the frame must be positioned repeatably in order to precisely control the amount of spring compression. To achieve this tight positioning control, we use an encoded servo-motor driven ball-slide to drive the frame.

It is critical that the six defining surfaces are contacted cleanly in a mechanism of this type. If the mechanism stops with only three, four or five surfaces contacted, the mirror position will be ill-defined. No amount of increased driving force will cause the mechanism to engage the other defining points. This is because the opposing forces at the surfaces are proportional to the normal force, which in turn is proportional to the driving force. Thus, for a given coefficient of friction, the success of the mechanism is a function only of the geometry and not the driving mechanism. We undertook an analysis of the friction forces at each ball-kinematic contact surface so as to predict the viability of this design configuration. The complete friction analysis is detailed in the literature by Sheinis et al. (1999a).

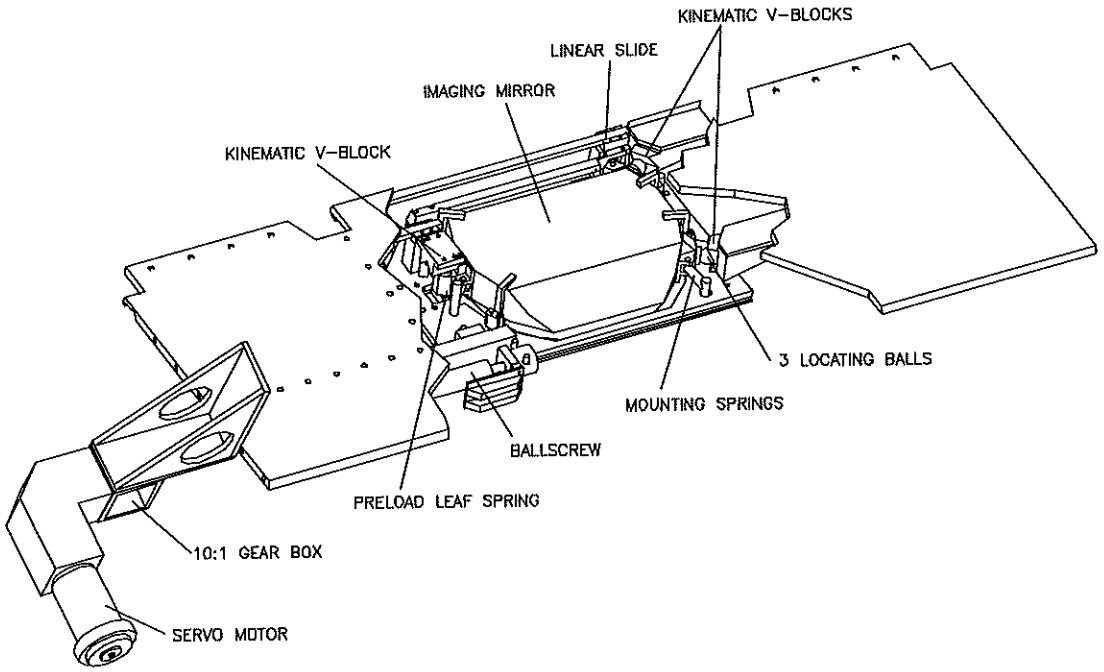

Fig. 14.— Mirror stage assembly, mirror-in.

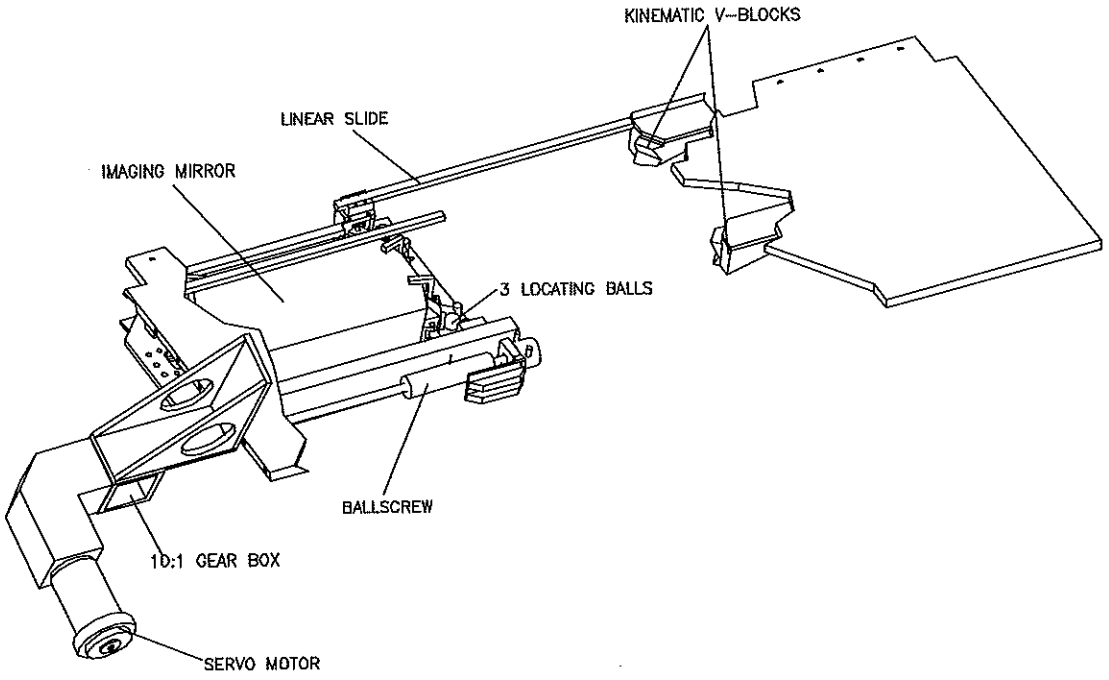

Fig. 15.— Mirror stage assembly, mirror-out.

2.3.3. Repeatability Analysis

Residual non-repeatability in the angular location of the mirrors can be attributed primarily to three factors: 1) variations in the compression of the ball/kinematic flat due to variations in the Hertzian contact stress; 2) bending of the Invar glue pad assemblies; and 3) deformation of the glass optic itself. We calculate the magnitude of each of these effects in order to estimate the repeatability of the device.

A detailed analysis of the Hertzian contact stress is presented in the literature Sheinis et al. (1999a). From this analysis, the Hertzian contact stress ranges between 48,000 and 144,000 PSI depending on the orientation of the gravity vector. The corresponding maximum compression range is 1.4 microns at the ball contact point. This corresponds to an angular error of $0''.96$ for our system geometry.

In addition, with such a high contact stress, we needed to be concerned about material selection, so as not to yield the material. We chose Speedstar AISI type M2 (UNS T11302) high speed steel, hardened to Rockwell 62, with a yield stress of over 400,000 PSI, for the kinematic V-blocks. Also, we used hardened (SS 1142) tooling balls that were hardened to Rockwell 60, with a yield stress of 285,000 PSI.

Mechanical deformation of the Invar glue pad assemblies was modeled as a simple cantilevered beam. Thermal deformations of the glass due to the glue pad were modelled analytically following Iraninejad et al. (1987). Mirror deformations due to three-point support were modeled analytically following Nelson et al. (1982). All these deflections were found to be well below the requirements set by the error budget.

2.3.4. Bench Testing and Performance Analysis

In order to test the system it was assembled prior to the rest of the spectrograph. An interferometer was used to measure the deformation of the mirror and the repeatability of the system. With this technique, no visible deformation was observed in the mirror (to $\lambda/10$) and the repeatability was observed to be better than $1\farcs0$ in a single gravity orientation.

Once the entire spectrograph was assembled, we were able to make repeatability measurements *in situ*. This was done by placing a machined pinhole in the slit plane to create an artificial star. Using a calibration line lamp, the image position on the CCD was recorded in all three spectrograph-operating modes before and after the individual mirrors were engaged for a single orientation of gravity. Next, the spectrograph was mounted in a Cassegrain simulator, which allowed us to tilt it, thereby inducing the different gravity orientations. We tested the repeatability of the both stages under these conditions and observed sub-arcsecond performance in all gravity orientations.

2.4. Camera Subsystem

The camera optical design is shown in Figure 16. It consists of ten lens elements in five lens groups. The camera has an effective focal length of 308 mm. It has an entrance aperture diameter of 287 mm and a final plate scale of 97.7 microns/arcsec on the sky. The collimated beam diameter is approximately 160 mm. The camera's effective f/ratio in imaging mode is thus f/1.93 and slightly faster in spectroscopic modes due to anamorphism.

The camera design is all-spherical and it includes two large CaF_2 lenses. Group #1 is a doublet, group #2 is a CaF_2 singlet, groups #3 and #4 are triplets while group #5 is the field flattener/dewar window. The elements in groups #1 and #3 are optically

coupled with a fluid (Cargille laser liquid Type 5610 $n_D = 1.5000$) to minimize internal reflections. The elements in group #4 are greased together with Dow Corning Q2-3067 optical couplant. The six larger elements were fabricated by TORC and the 4 smaller elements were fabricated by Cosmo Optics Inc., (Middletown, NY). Broad-passband AR coatings were applied by Coherent Auburn Division (Auburn, CA).

The ESI optical design is complicated by the fact that a wide variety of pupil anamorphic factors and effective entrance pupil distances are presented to the camera's entrance aperture by the three operating modes. (In practice, the camera design was slightly compromised in the imaging and LDP modes so as to favor the echellette mode). Nevertheless, the echellette mode remains the most severe test of system image quality.

In order to produce detailed sensitivity analysis, individual lens elements were perturbed axially, radially, and in tip/tilt within the computer model. The perturbed camera model was ray traced within the ESI spectrograph numerical model in echellette mode at 50 different wavelengths, covering all 10 orders. In order to determine the sensitivity coefficients of the camera , the perturbed system was compared to the unperturbed system. The worst centroid location change and worst increase in the rms spot-size diameter (D_{rms}) were noted. A similar analysis was performed for the lens groups. After moving entire groups, we calculated the resulting centroid motion and change in D_{rms}.

These sensitivities were used to estimate manufacturing and assembly tolerances for the mechanical components such that the expected summation of image errors (added in quadrature) was comparable to the residual aberrations in the optical design. In addition, the sensitivity data allowed setting of a lens-motion tolerance in terms of the total allowable image motion for the different gravity orientations.

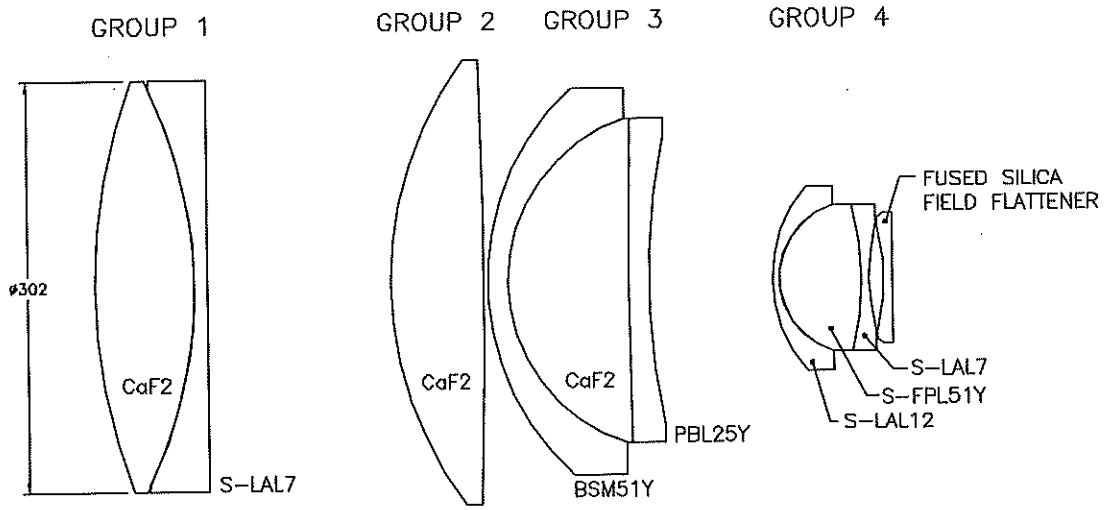

Fig. 16.— Camera optical design.

2.4.1. Camera Opto-Mechanical Design

The camera mechanical system (CMS) for ESI was designed by J. Alan Schier Co., (La Crescenta, CA 91214) and fabricated by Danco Machine, DPMS Inc. (Santa Clara, CA). The CMS is shown in Figure 17 . It consists of four cells supported within a single large barrel. The mass of the entire camera assembly, consisting of the CMS and the lens elements, is approximately 125 kg. The individual cells with their respective lens elements have masses ranging from 5 to 30 kg. The cells locate radially against locating surfaces (lands) on the barrel inner wall and axially against athermalizing spacers. Each cell consists of an aluminum housing, radial athermalizing spacers and a compressive preload spring. Each of the two oil-coupled cells also contains an oil sealing reservoir system. The lens element spacings within the oil-coupled cells are maintained by 0.10-mm Mylar spacers, placed between the lens elements at their edges.

We now describe the major features of the opto-mechanical design:

Athermalization

In principle, axial-athermalizaton would require that the effective system magnification as well as the focal location relative to the CCD are invariant over the operating temperature range. As part of the sensitivity analysis we calculated a linear relationship between the two intergroup spacings, such that the optical impact of small perturbations (all axial distances, changes in curvature and changes of refractive index) was minimized with regard to magnification and focal location. In practice we found that the compensation was imperfect. We decided to emphasize focal position over image scale change.

From these considerations, we determined the effective coefficients of thermal expansion (CTE) between the two individual groups so as to provide the required spacing changes

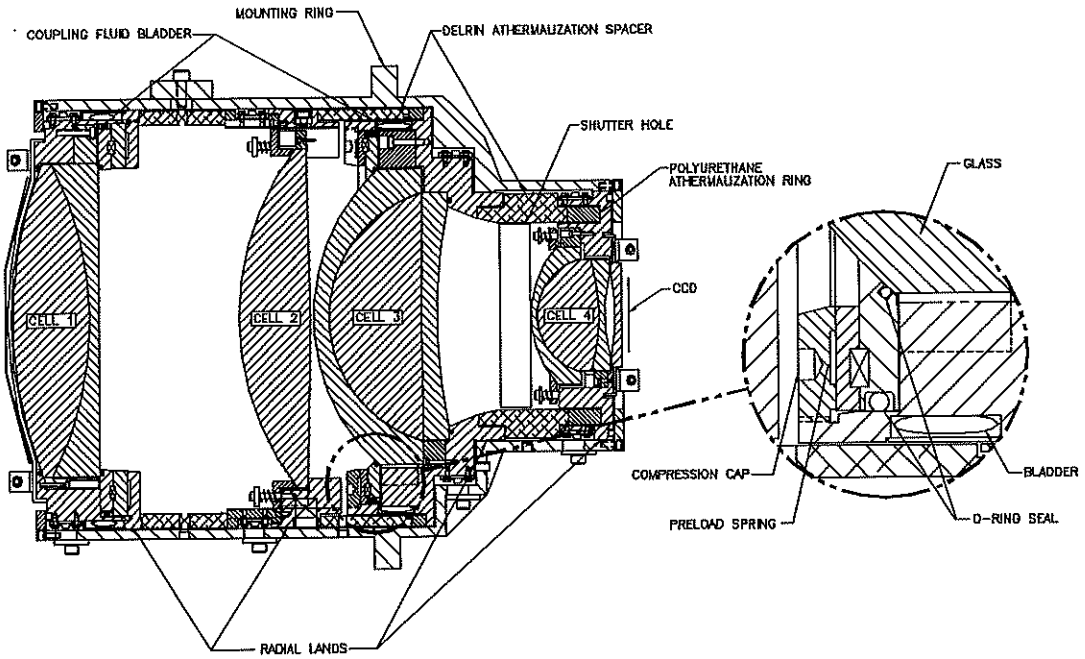

Fig. 17.— Camera opto-mechanical design.

with temperature. These effective CTEs were achieved by using stacks of 3 materials, (aluminum, Delrin II and polyurethane) between cells 2 and 3 and between cells 3 and 4. A single material (aluminum) was adopted between cells 1 and 2 and between cell 4 and the dewar.

Actual material CTEs had to be measured in the laboratory and in some cases they differed substantially from the vendors' catalog values. In addition, simple material compression had to be considered in the material choice as the weight of the cells plus compression spring force contributed to a possible compressive force of up to 130 kg on the spacers.

The purpose of the radial athermalization is to maintain zero internal stress in all the optical elements over the entire survivability temperature range while maintaining an axial centration as prescribed by the sensitivity analysis over the operating temperature range.

To achieve this goal, a set of Delrin II pads was used to match material expansion with temperature. This expansion is due to the difference between the CTEs of the lenses and the aluminum housings. This concept is similar to that used in the LRIS camera Oke et al. (1994) on Keck I.

An additional factor of great concern is the effect of transient temperature changes. If the ambient temperature cools too rapidly, a thermally induced interference could occur within the cells. This results from the fact that the aluminum housings have thermal time constants of approximately 15 minutes while the lenses have thermal time constants as long as 120 minutes. At a temperature difference of 14 °C an interference occurs in cell #2. The other cells experience this at greater temperature differences. With this in mind, we have set 5 °C per hour as the maximum temperature change rate to be experienced by the camera under any circumstance.

Cell#2 Transverse Adjustment

From the sensitivity analysis we determined that a lateral adjustment of cell#2 could compensate for fabrication and assembly errors in other parts of the CMS. For this adjustment mechanism, a 0.5 mm passage was cut completely through the aluminum housing except for three transverse flexures. This cut effectively created an inner and outer housing which can be adjusted laterally relative to each other. This mechanism is seen in Figure 18.

Optical Coupling Fluid Control

Cells #1 and #3 contain an optical coupling so as to accomodate CTE differences between the lens elements and to minimize internal reflections. An o-ring seal is provided at each glass-aluminum interface. The o-rings are compressed to the minimum nominal-dynamic-seal specification (8%). The o-rings are compressed such that the optic locates directly against the aluminum land and the o-ring carries most of the load, while providing a seal.

A polyurethane bladder is used to accommodate volumetric changes of the coupling fluid within each cell. Possible reactivity of the optical coupling fluid with polyurethane and other substances was tested by Hilyard et al. (1999). They found no reactivity with the polyurethane bladder material.

2.4.2. Camera Integration

The camera integration procedure was developed with the aid of a set of simulated lens elements fabricated from aluminum. We practiced several times with the simulated lens elements until we were comfortable with the amount of manual handling required and the risks involved. With the exception of the translational location of cell #2, the

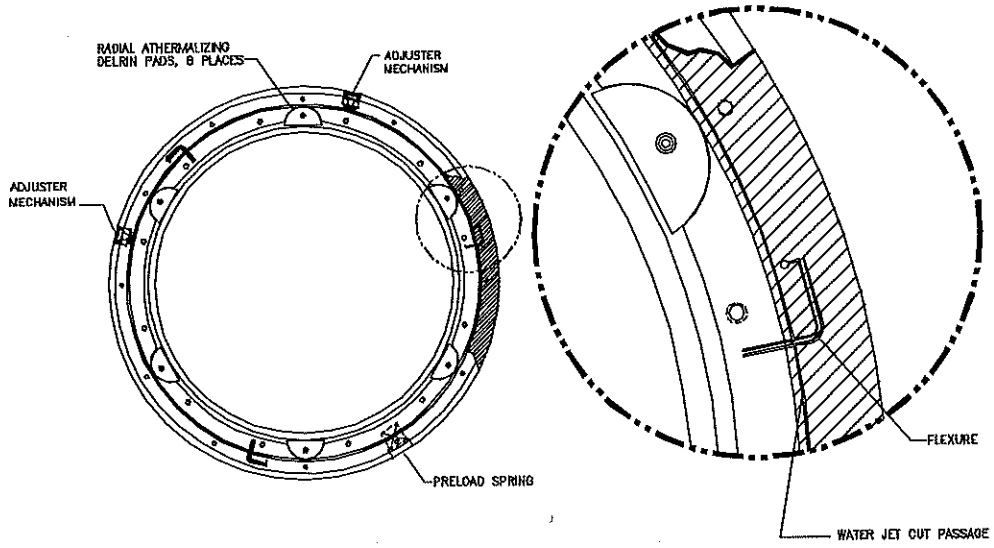

Fig. 18.— Cell #2, final adjustment mechanism.

camera's optical alignment is achieved by close-tolerance fabrication of the CMS. The radial locating surfaces within the cells, i.e., the inner radius of the Delrin II radial athermalizing spacers, as shown in Figure 17, were final machined to match the as-measured isothermal optic diameters plus a 0.025 mm radial clearance. This was done after the spacers were bolted into the aluminum housings in order to increase the centration accuracy of the hole relative to the outer housing diameter. The cells were assembled on a precision rotary table. Both the lens elements and housings were aligned to the rotary table by minimizing their horizontal and vertical run-out.

After the cells were assembled the index-matching coupling-fluid was added via a gravity feed system. This fluid had previously been placed into an evacuated bell jar to remove any dissolved gasses. Lastly, cell-land locations were measured relative to the lens vertices and axial spacers were cut to their final lengths. This final proceedure was done last to remove as much axial assembly error stack-up as possible.

2.4.3. Camera Bench Testing and Performance Analysis

After assembly of the camera, a battery of optical performance tests, including interferometric testing, polychromatic-point-spread function measurements and back-focal-distance measurements were carried out. The results of these tests compared well with the predictions from the lens design. For example, the polychromatic (Wratten 54) RMS spot diameter on-axis was measured to be 13.7 microns, as compared to a predicted rms spot diameter of 12.5 microns. These tests are discussed in detail in Sheinis et al. (1999b).

2.5. Detector and Controller

The ESI detector (device W62C2) is a MIT/Lincoln Labs CCID20 high-resistivity CCD (?) with 4096 rows and 2048 columns of 15-micron square pixels. It has two significant cosmetic defects in the lower-left (blue) quadrant. A glowing pixel at column 85 of row 3895 contaminates a (10 by 10) pixel area, while 18 adjacent bad columns on the bottom $\frac{1}{3}$ of the device affect order 14 from 4460 to 4565 Å. However those wavelengths are available outside of the free spectral range in order 13. Additionally, there are 13 traps and several horizontal and vertical micro-fractures which are the result of the high-temperature processing of the CCD wafer.

There are readout amplifiers at both ends of the serial register and both are operational. Measured deviations from flatness are 18 microns peak to valley at the normal operating temperature of $-120°.0$ C. At that temperature, the on-chip amplifier read noise as measured in the laboratory is 2.3 electrons for one amplifier and 2.6 electrons for the other. The measured readout noise for each amplifier increases by 0.3 electrons when: The CCD Dewar is mounted in ESI; The ESI instrument is mounted on the Keck II telescope, with all of the motorized stages within ESI powered up and operating; The telescope is tracking.

Operating at $-120°.0$ C, the dark current is 2.1 electrons/pixel/hour in non-MPP mode. At that temperature, the various wavelength-dependent specifications for the CCD are shown in Table 3. Note, these MIT/LL devices are not capable of MPP mode operation.

The CCD controller for ESI is a San Diego Sate University second-generation device (SDSU2) developed by Leach et al. (1998). It provides both a low-gain and a high-gain mode of operation. While the pixel full-well of this CCD is 105,000 electrons, the achievable full-well is limited by the 16-bit resolution of the analog to digital conversion. Table 4 shows the achievable full-well as a function of the selected gain.

Table 3: CCD QE and Fringing

Wavelength	QE %	Fringing %
3200 Å	10.2%	
4000 Å	60.8%	
5000 Å	82.4%	
6000 Å	80.3%	
7000 Å	77.1%	
8000 Å	68.9%	12.0%
9000 Å	45.0%	15.0%
10000 Å	11.3%	30.0%

Table 4: Achievable Full-Well Versus Gain

Mode	Gain	Achievable	% of Pixel Full-Well
low gain	1.30 e-/DN	84,500 e-	80
high gain	0.52 e-/DN	31,000 e-	30

The controller also provides a software-selectable choice of three different readout speeds. However nearly all observations are performed using the fastest of the three speeds. Table 5 provides the details of the per-pixel timing for the fastest and slowest speeds while Table 6 shows the serial charge transfer efficiency for this CCD as a function of the selected readout speed. Note that the parallel charge transfer efficiency for this device is 0.9999999 (virtually perfect) at $-120°.0$ C for all readout speeds and the readout noise is the same at all readout speeds. While the slow speed readout mode is seldom used, it does provide for nearly perfect serial charge transfer efficiency at the cost of significantly increased readout time.

The CCD controller uses two video processing boards. This was done to avoid a problem with crosstalk between the two channels of the same board. While there is crosstalk of 1 part in 60,000 between the two channels of the same board, there is no detectable crosstalk between the video channels on separate video processing boards. Neither is there any detectable crosstalk between the two amplifiers of the CCD nor between the preamplifiers in the signal chain for normally exposed images.

The controller provides software-selection of single-amplifier mode readout from either of the two on-chip amplifiers, or dual-amplifier readout using both amplifiers. In normal operation, dual-amplifier readout is used. Table 7 provides the readout times for various operating modes.

While the controller supports both horizontal and vertical on-chip binning, it should be noted that on these MIT/LL CCDs, the full-well capacity of the pixels in the serial register and in the summing well is not significantly larger than the full-well of the pixels in the imaging area. Unfortunately, the limited well depth of the serial register pixels and the summing well significantly constrain the exposure levels that can be utilized when using on-chip binning.

Table 5: Per Pixel Timing Versus Readout Speed

Readout Mode	Sampling Time (Baseline+Video)	Serial Width	Pixel Overlap	Pixel Freq Period	Amplifier
fast	1 μ sec + 1 μ sec	3 μ sec	1 μ sec	7.2 μ sec	139 Kpixels/sec
slow	5 μ sec + 5 μ sec	17 μ sec	7 μ sec	25.2 μ sec	40 Kpixels/sec

Note. — Serial transfer is overlapped with video processing

Table 6: Serial Charge Transfer Efficiency vs Readout Mode.

Readout Mode	Per Pixel Time	CTE	% loss after 1024 transfer
fast	7.2 μ sec/pixel	0.99998	2.0%
normal	10.5 μ sec/pixel	0.99998	2.0%
slow	25.2 μ sec/pixel	0.999996	0.4%

Note. — Serial transfer is overlapped with video processing

In order to eliminate residual image and to minimize the area of the CCD that is affected by the hot columns in the lower-left quadrant, a three-pass erase scheme is used. The first pass involves parallel-shifting approximately 100 rows using higher-amplitude parallel clocks (+2 volts to -8 volts). This eliminates residual image but the higher-amplitude parallel clocks generate some spurious charge into the imaging area. The second pass consists of a standard erase cycle using normal-amplitude (+2 volts to -6 volts) parallel clocks in which charge is parallel-shifted up toward the serial register and then shifted serially out to the output amplifiers. Note that these parallel-clock waveforms utilize trapezoidal-shaped waveforms (with 100 microsecond linear rise and fall times) to virtually eliminate spurious charge generation. While this second pass effectively erases the CCD and eliminates the spurious charge introduced by the first pass, it also carries charge from the hot columns in the bottom quadrants toward the serial registers, thus contaminating those columns in the upper quadrant of the device. In the third pass of the erase cycle, the direction of parallel transfer is reversed and charge is shifted away from the serial register, thus clearing the affected columns in the upper quadrant and confining the effect of the hot columns to the lower quadrant of the device. Because of this three-pass erase scheme, 12 seconds are required to erase the CCD.

2.5.1. CCD Dewar

The Dewar holds approximately 4 liters of liquid nitrogen which is available to cool the CCD to $-120°.0$ C. The hold-time for the half-full vessel is approximately 20 hours. The CCD is supported in the Dewar housing by a hexi-pod structure. This structure provides a very rigid support and thermal stand-off for the CCD. The flexure of the cryogenic container is isolated from the CCD by a flexible copper braid that connects the chip to the cold finger. The vacuum housing with cyro-container is kinematically mounted to the

back flange of the camera. The kinematic mount has three adjustable screws to tip, tilt and piston the CCD for alignment to the focal plane. The Dewar can be removed from the camera and reattached to the kinematic mount without disturbing the Dewar alignment. The alignment of the spectra on the chip is also adjustable by means of a cam which rotates the Dewar about the optical axis. Like the piston and tip/tilt adjustment, this is a one-time only adjustment that is preserved if the Dewar is removed.

2.6. TV Guider

The guider system design is pictured in Figure 19. The guider system combines a 200-mm Canon lens, a Photometrics PXL camera with a 1K by 1K (24-micron pixels) detector and a Melles Griot shutter to produce a $4\farcm0 \times 4\farcm0$ f.o.v. on the sky. The guider f.o.v. includes a $\farcm2 \times 4\farcm0$ portion of the instrument f.o.v., with the remainder of the guider field being located on a fixed mirror adjacent to the slit masks. The guider focus is operated by a motor which drives a toothed-belt attached to the manual focus ring of the Canon lens. The guider system also has an eight-position filter which can accommodate 50-mm square filters (1-mm to 10-mm thicknesses).

In addition to the f.o.v. requirements and the functional requirements (which included the provision of a remotely controlled focus and filter wheel assembly), the TV system needed to meet a strict flexure specification. This was because the system guides by centroiding on an offset image. Due to mechanical constraints imposed by the position of the spectrograph optics, the chosen guider field is more off-axis then the scientific field. The echellette slits are tilted out of the focal plane to move the TV system out of the incoming beam. This configuration requires that the guide stars in the TV mirror do not come to focus on the surface of the mirror. Therefore, they cannot benefit from reference marks on the mirror surface. For this configuration, any flexure in the TV system optical

Table 7: Readout Times for Full Chip

Amplifier Mode	Fast Readout	Slow Readout	Binning
Dual amplifier	39 seconds	128 seconds	none
Single amplifier	70 seconds	240 seconds	none
Dual amplifier	23 seconds	67 seconds	2 by 2
Single amplifier	38 seconds	122 seconds	2 by 2

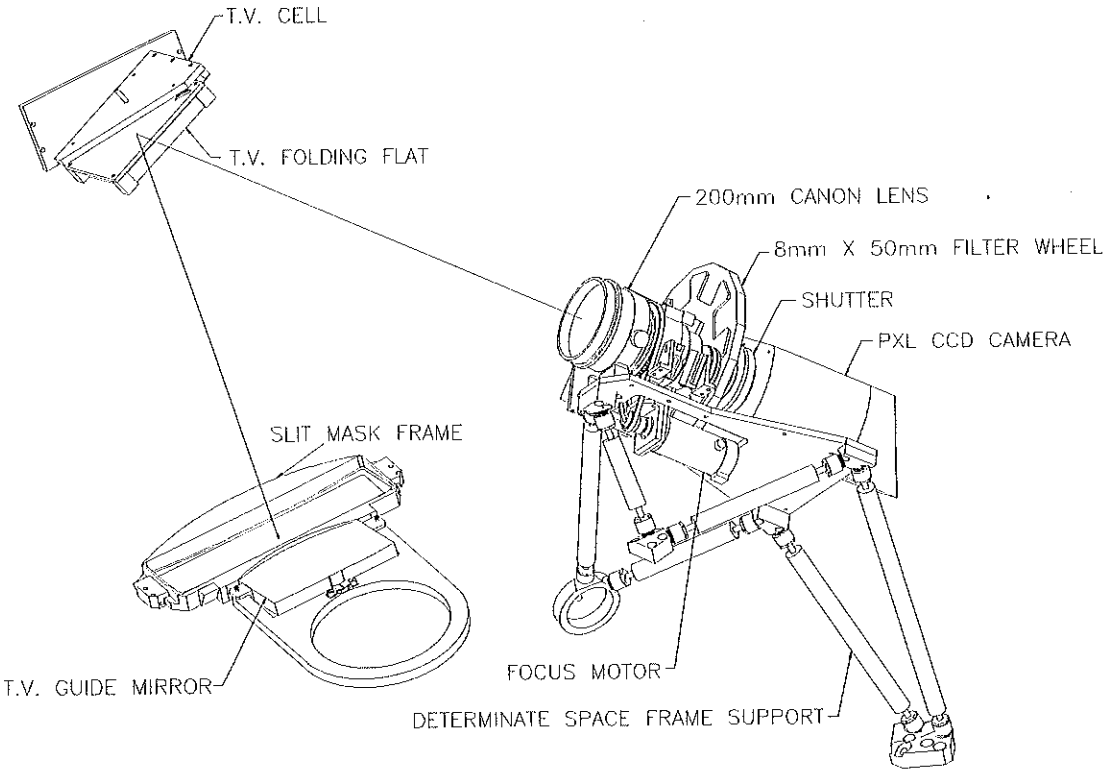

Fig. 19.— ESI guider system.

path will introduce a gravity dependent error in the telescope pointing. For these reasons, a specification of $\pm 1/2$ pixel of relative flexure for any 2-hour observation was set.

The guider components are mounted to a common baseplate in order to simplify the structure. In addition to the items described above, the system includes a detachable kinematic baseplate for the PXL camera shown in Figure . This feature was necessary to allow an alignment laser to be attached quickly and accurately to the optical axis for the rough alignment.

We adopted the same philosophy for the guider support as for the rest of the instrument. The baseplate was designed to have three nodes for attachment to the main instrument structure. Six 25-mm diameter x 4.75-mm wall thickness struts form a determinate structure to support the guider package. Each strut is fitted with M6 x 0.75-mm left- and right-hand threaded studs and with ball sockets at each of its ends. Alignment of the system is accomplished by rotating the struts to change their lengths. Once the alignment is close to the final settings, locking nuts are tightened to form a rigid, hystersis-free joint at the socket.

Minimization of gravity-induced flexure was accomplished with an FEA model of the entire instrument. Sensitivity to the strut-stiffnesses was investigated by running multiple analyses and varying only the cross sectional area of the TV struts. The optimized solution prediction for flexure was ± 0.14 pixels for any two-hour observation.

The stiffness of the TV structure was confirmed in the laboratory by measuring the relative motion of the guider images of a test target attached to the offset-guider mirror, as the spectrograph was moved in altitude and rotation angle via a Cassegrain-mount simulation fixture. These tests where later repeated on the telescope and the flexure was found to be below the 1/10 pixel measurement limit of our technique.

2.7. Calibration Source

Each of the two ESI calibration systems consists of one or more source lamps, condensing/relay optics, a fiber-optic light guide, a projecting optic and a diffusing panel common to both systems. The first system contains lamps for neon, argon, mercury-neon and a quartz-continuum source. The second contains a low pressure copper-argon line lamp. Both systems may be used simultaneously which allows for independent selection of any combination of source lamps. The lamps are physically separated and thermally isolated from the primary optical path of the spectrograph in order to limit internal seeing. The fiber-optic light guide delivers light of appropriate wavelengths to a diffusive reflecting panel located on the back of the spectrograph entrance hatch. The light is then relayed through the spectrograph to the CCD.

3. Structure

3.1. Requirements

The design of the ESI instrument structure was constrained by weight, center of gravity, volume, and stiffness requirements, as well as budget and schedule considerations. Cassegrain-mounted instruments for Keck must attach to an instrument module, which serves as a carriage for loading the instrument on the telescope and a storage cart when the instrument is not in use. The Cassegrain module also provides a bearing for field de-rotation and mechanical, electronic and data interfaces between the telescope and the instrument.

The external requirements for the instrument include: (1) A mass limit of 2425 kg for the instrument+module unit; (2) The instrument+module center of gravity must be located *at the center* of the Cassegrain module rotation bearing; (3) The instrument must stay within a space envelope which is roughly cylindrical in shape, 2.0 meters in diameter

and 2.5 meters long. Figure 20 shows a cut-away view of the instrument space envelope, Keck Cassegrain module, the esi structure and the locations of most of the optics.

The structural stiffness requirements are crucial to the performance of the instrument. A detailed sensitivity analysis of image size and motion, as functions of translations and rotations of the individual the optical components, was used to set the allowable deflections and rotations in the structure. The dynamic response of the structure (first resonant frequency) was assigned a minimum value of 30 Hz.

Based on experience with the Keck Low-resolution Imaging Spectrograph (LRIS) (Oke et al. 1994), it was known that significant deformations of the Cassegrain module and rotator bearing were due to forces passed though the module mounting points by deflection of the Keck primary mirror cell. Given the over-constrained connection between the telescope and module, the decision was made to use a determinate space frame for the esi instrument structure and to attach it kinematically to the Cassegrain module. In keeping with the instrument budget and schedule constraints, we used steel as the frame material.

3.2. Structure Overview

The center of the ESI structure is a triangular mainframe which provides the foundation for the sub-structurals and the connections to the rotator bearing. Extending below the mainframe is the collimator structure which supports the tip/tilt and piston actuators carrying the collimator mirror. Details of the support and drive of the collimator mirror flexure-control are described in section 2. The optics support structure (OSS) and the slit area stages are located above the mainframe. The OSS is mounted to the mainframe via a determinate structure, the slit area stages are mounted via an over-determined structure. The final design of the mainframe, collimator structure, and connections to the Cassegrain

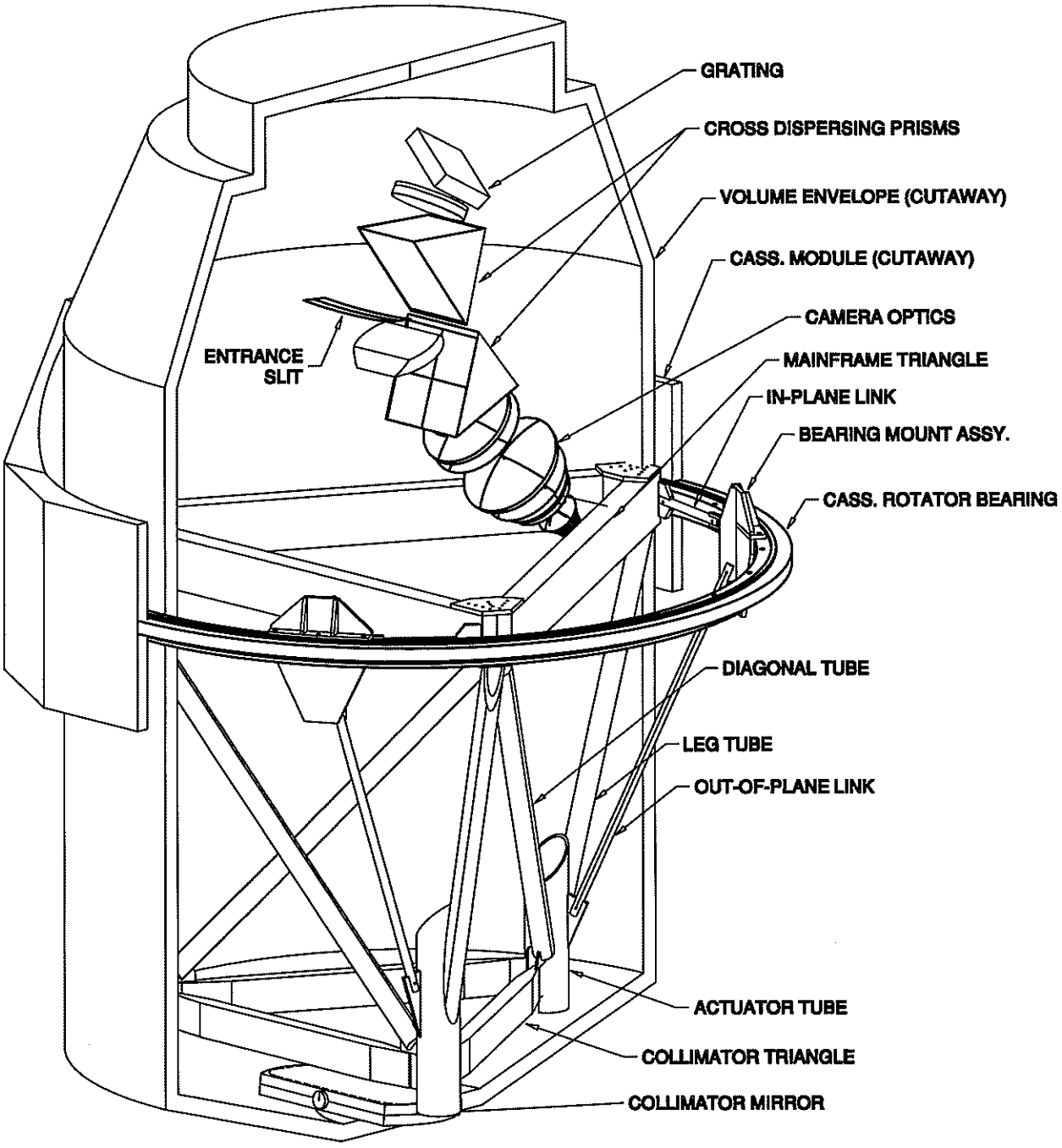

Fig. 20.— The ESI mainframe and Cassegrain rotator bearing.

rotator are shown in Figure 20.After preliminary conceptual designs for the structure and links were completed, finite element modeling, using the ANSYS program, was used to examine the static and dynamic response of the structure.

The primary concern about the static response of the structure was that flexure-induced tilts of the collimator mirror support points, relative to the mainframe, be within the allowable values (3.″0). Hence, analyses were carried out for the three orthogonal gravity orientations (**X**, **Y**, and **Z**), and support point tilts were calculated from the resulting structural deflections.The worst-case tilts of the collimator triangle were 1.″9, well within the specification. Peak deflections of the collimator mounting points occurred with gravity parallel to the optic axis, and had a peak value of 136 microns. The deflections in this orientation corresponded to a "unscrewing" of the structure relative to the mounting points on the rotator bearing. These deflections had little affect on the optical performance as the motion of the collimator is primarily rotation about its parent axis.

The primary goal for the dynamic response of the structure was that its first resonance be significantly higher than the lowest resonant frequencies in the telescope structure which are of order 10 Hz. As mentioned above, the maximum static deflection in the structure was calculated to be 136 microns. Assuming the well-known spring-mass equivalent system, the first resonant frequency of the structure can be calculated directly from this deflection. This first resonant frequency was 42 Hz, well above that for the telescope.

3.3. Optical Sub-Structure

The Optical Sub-Structure (OSS) was designed as a bolted box to which the grating, fixed prism, moving prism, imaging mirror, low-dispersion mirror and the camera attach. The decision to use this approach rather than a pure space-frame approach was driven by

the complications imposed by a three-mode instrument. The large moving masses (prism and two mirror assemblies) coupled with the tightly packaged and folded optical path made the box solution very appealing. All optical assemblies were designed to attach to the OSS in quasi-kinematic ways to insure that deformations of the box (OSS) would only cause free-body motion of the sub-assemblies rather then deformations. Two methods of attachment were used depending on the optic.

The two fixed optics, one prism and the camera where attached to the OSS by hexapods. The connection points (nodes) were chosen to be at the intersection of at least two plates so that reaction force in the OSS structure could be provided by the vector sum of sheer forces in the plates. Stated in different terms, the OSS was designed in a manner that insured that the plates could not react in any bending mode.

The OSS's main performance requirement was the instrument flexure specification. Because it held all spectrograph optics except the collimator, any differential rotation of the OSS's optical axis relative to the collimator would result in large image motion at the CCD. To complicate matters, this assembly is very massive and it one produces the largest component of the instrument flexure. Thus the most significant reduction in total flexure was accomplished by minimizing the OSS flexure. For this reason a hexapod structure was used to attach the OSS to the mainframe. It addition to its inherent large stiffness, the hexapod structure also provided an easily alignable support for the OSS.

3.4. Filter and Slit Wheels

ESI uses a triple-wheel filter/slit assembly located near the Cassegrain focus to hold a variety of removable slit and filter components. Each wheel has five bays which can accommodate as many as three 2.'0 by 2.'0 filters each. Only the top-most wheel is *at* the

telescope focus. It can hold as many as four different long-slits and/or multi-slit plates, as well as the full complement of echellette slits. In practice one bay is left empty to allow for direct imaging. Each wheel of the triple-wheel assembly consists of a metal-belt-driven wheel with a dual-closed-loop encoder for angular location control. The motor and drive system uses a Galil 50-1000 motor to power a 50 to 1 harmonic drive. Additional drive reduction exists due to the drive-wheel to filter-wheel diameter ratio. The ratio between the two wheels is 32.9 to 1 (drive to driven). The second loop of the servo system is encoded by a 5-micron Renishaw optical encoder. For the filter wheel diameter of 790 mm, the Renishaw encoder provides 2.″6 of angular resolution.

4. Flexure Minimization

In the following section we report on the mechanical performance and flexure minimization of the instrument. The predicted mechanical performance is based on the combination of a detailed set of optical sensitivities from the optical design analysis and a finite element analysis of a slightly simplified structure model.

The flexure compensation system is passive a mathematical representation of previuoslyobserved image motions to predict the expected image position for any altitude and azimuth location of the spectrograph. The flexure compensationis provided open-loop by actively tilting the collimator mirror, so as to compensate for the combined motions of all the other optics in the optical train. We report on the details of this modeling and the results of the flexure testing in the laboratory and at the telescope with and without flexure compensation.

4.1. Passive Flexure Performance

Because most of the structures of the instrument are determinant space-frames, it is possible to model the instrument precisely with a relatively simple finite element model (FEM). The goal of this analysis was to use predicted motions of all the optical components as a function of gravitational orientation so as to predict the resulting image motion. To accomplish this task, we calculated the optical sensitivity of the final image location to motions of each optic individually in all six of its degrees of freedom. We then combined the FEM predictions of the optic motions for various gravity orientations with these signed sensitivities to get the resultant image motion at the detector for any orientation of ESI. This FEM was then used to optimize the structure for minimum image motion at the detector during the design process.

4.1.1. Requirements

The passive flexure goal was set at ± 1/2 pixel for any two-hour observation. Predictions of the real-world performance of ESI based on the FEM and laboratory tests were not easily and directly compared to this specification. We modeled and measured flexure in an orthogonal coordinate system, (altitude and instrument position angle) but transforming that into what one can reasonably expect during the worst-case observation would require searching through all possible two-hour integration paths on the sky. This would need to be repeated *for every change in the FEM.* For simplicity, we chose to minimize the overall flexure with respect to our orthogonal coordinate system, rather than in terms of image trajectories on the sky (altitude and azimuth).

4.1.2. FEA Model

Having never attempted to predict the total image motion in a spectrograph as a function of the gravity vector with a finite element analysis (FEA) model, the philosphy we chose was to formulate a relatively simple macro-structure model of the instrument while doing our best to design micro-structures that had stiffness well beyond the expected stiffness of the instrument macro-structure. This allowed us to ignore the details of the micro-structures in the FEA macro-structure model. This model was primarily composed of beam elements to represent the space-frame structures and shell elements to simulate the performance of the OSS. The grating, mirrors and prisms were modeled as point masses located at their respective centers of gravity. The predicted motion of each of these point masses was entered into a spreadsheet and multiplied by the signed sensitivities to predict the total instrument flexure. We used the image motion predicted by this speadsheet to locate and remedy several weaknesses in the design.

4.1.3. Analysis and Testing

During the in-laboratory flexure testing of the assembled instrument, we discovered an additional major source of image motion. This image motion was due to coupling of Cassegrain rotator bearing errors into the instrument structure. For these tests ESI was assembled and installed into a test fixture which produced the variations in position angle and elevation that the instrument would see in the telescope. In the initial design, the attachment of ESI to the bearing was purposely made compliant to mitigate against these bearing deformations such that they could not pass moments into the structure. However, testing of the flexure at zenith showed repeatable image motion with a two-pixel amplitude over 360°.0 of rotator motion. In this configuration the gravity vector does not change relative to the instrument so bearing induced deformation was the only likely culprit.

Rather than attempting to model the bearing in detail, we approached the problem by minimizing the safety factors of the instrument connection. By reducing the diameter and increasing the length of the three short struts that lie in the bearing plane we reduced substantially their stiffness, while maintaining an adequate safety factor. We obtained a similar result with the out-of-plane struts by simply decreasing their diameters.

Testing of the new struts showed a large reduction in the bearing-induced flexure. Tests at zenith for a 360°.0 rotator rotation showed image motion of less than 1/2 pixel. Other smaller problems were identified and fixed during the testing which helped to reduce the instrument flexure to a final rms value of ± 0.25 pixels for zenith tests. Overall flexural performance is described in the next section.

4.2. Active Flexure Compensation

4.2.1. Overview

All Cassegrain spectrographs suffer from gravitationally-induced flexure to some degree. While such flexure can be minimized by careful attention to optical and mechanical design and fabrication, further performance improvements can be achieved if the spectrograph has been designed to minimize hysteresis and has active compensation for any residual flexure. ESI compensates for such residual flexure via its collimator mirror. The collimator is driven by three actuators that provide control of collimator focus, tip, and tilt. The ESI flexure compensation system (FCS) software utilizes a mathematical model of gravitationally-induced flexure to periodically compute and apply (open-loop) flexure corrections by supplying the required tip, tilt and focus motions to the collimator see Kibrick et al. (2000b). Although the flexure model is recalculated at a 1 Hz. rate, corrections are not applied until the accumulated image motion reaches 0.1 pixel in magnitude so as to avoid

unnecessary use of the collimator actuators. All three actuators are updated in parallel to minimize response time and mechanical stress on the collimator mechanism. Separate flexure models are used for each of the three spectrograph modes (echellette, low-dispersion and imaging).

The ESI FCS only compensates for those errors which can be modeled in terms of gravity-driven flexure. Non-modeled errors include those which might result from hysteresis, from changes in temperature across the instrument structure, from lost motion in optical stages, from residual lens-element movements in the camera and from small zero-point shifts which are observed whenever the instrument is removed from and re-inserted into the telescope.

The first operational test of the FCS system took place during instrument commissioning at the Keck II telescope (Mauna Kea summit) in September 1999. The flexure model was refined during subsequent engineering runs in October and November. The system became fully operational for science observing at the end of 1999 and it is now in routine use. The observed image motion due to flexure with the FCS active is not more than a few tenths of a pixel for a typical long exposure.

4.2.2. Image Motion vs Collimator Motion

Measurements of image motion versus collimator motion were obtained in all three instrument modes to determine the relevant transformations and to verify that the system operated linearly. We measured the image motions induced by individually moving each actuator by known amounts. Since there are three actuators but only two axes of the CCD (rows and columns), motion of a given actuator generally results in translation of the image in both axes of the CCD. These measurements verified the linearity of the system and

determined the effective gain of each actuator relative to the two axes of the CCD.

However, due to anamorphic distortion from the two cross-dispersion prisms in each of the two spectroscopic modes, the actual gain is not constant across the detector. In order to simplify the control algorithm, a specific image feature near the center of the detector was selected as the central reference for each instrument mode. The gains for each actuator were then determined for each instrument mode using their respective reference features. These same reference features were later used when determining the image motions induced by spectrograph flexure.

4.2.3. Image Motion vs. Spectrograph Orientation

Measurements of image motion induced by spectrograph flexure were obtained with the instrument and rotator module installed in the Keck II telescope. Line lamp calibration spectra were obtained in the two spectroscopic modes and images of the echellette slit were obtained in imaging mode. The telescope was stepped in elevation between 0, 30, 60, and 90 degrees. At each of these four elevations, calibration data were obtained at 17 different rotator position angles, sampling two full revolutions (one clockwise, one counterclockwise) in increments of 45 degrees of rotation. All flexure measurements were made using the same central reference features for each mode as were used to calibrate the actuator gains.

The results of the flexure measurements obtained during the October 1999 engineering run are shown for all three instrument modes as Figs. 21, 23, and 25. Note that in low-dispersion mode, the dispersion direction is parallel to the rows (or X axis) of the CCD, while in echellette mode, due to the grating cross-dispersion, the dispersion direction is parallel to the columns (or Y axis).

These plots show an unexpected result. If the telescope is pointing at the zenith, the

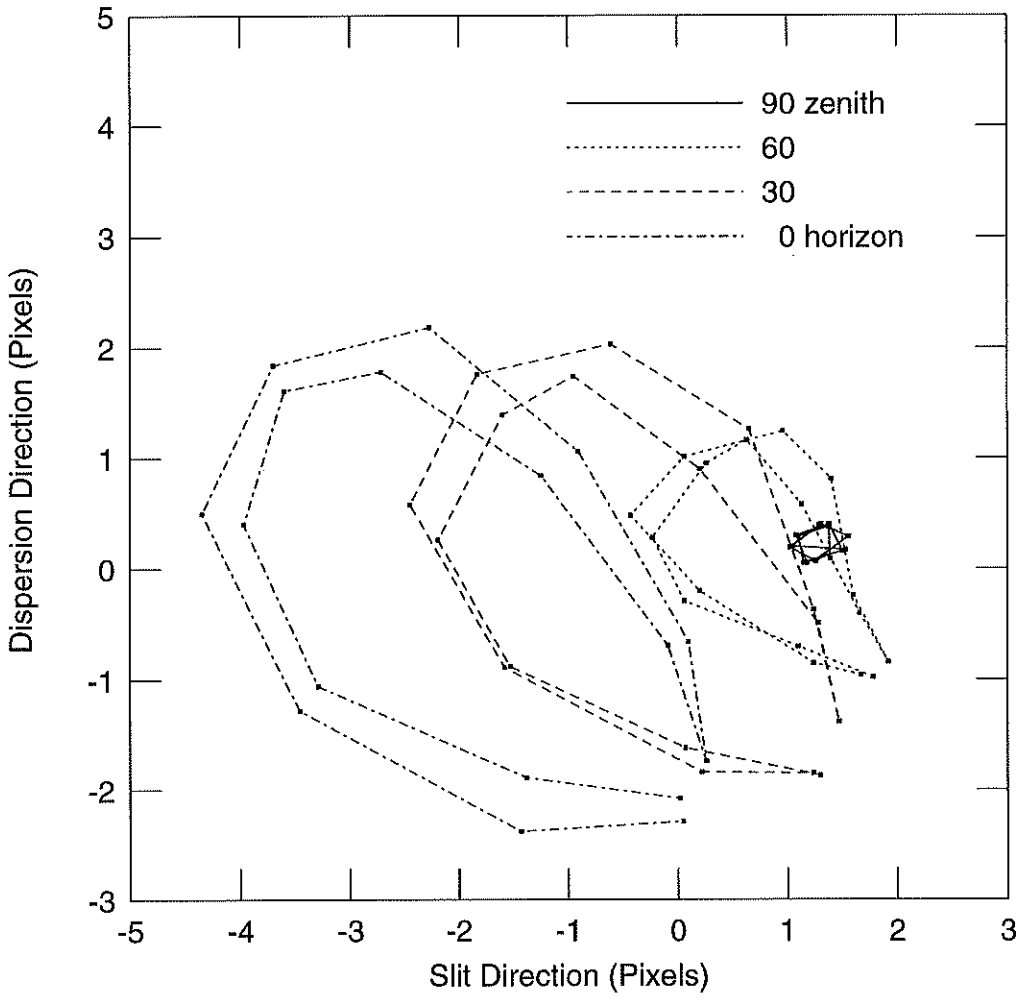

Fig. 21.— Flexure: Echellette mode (10/1999)

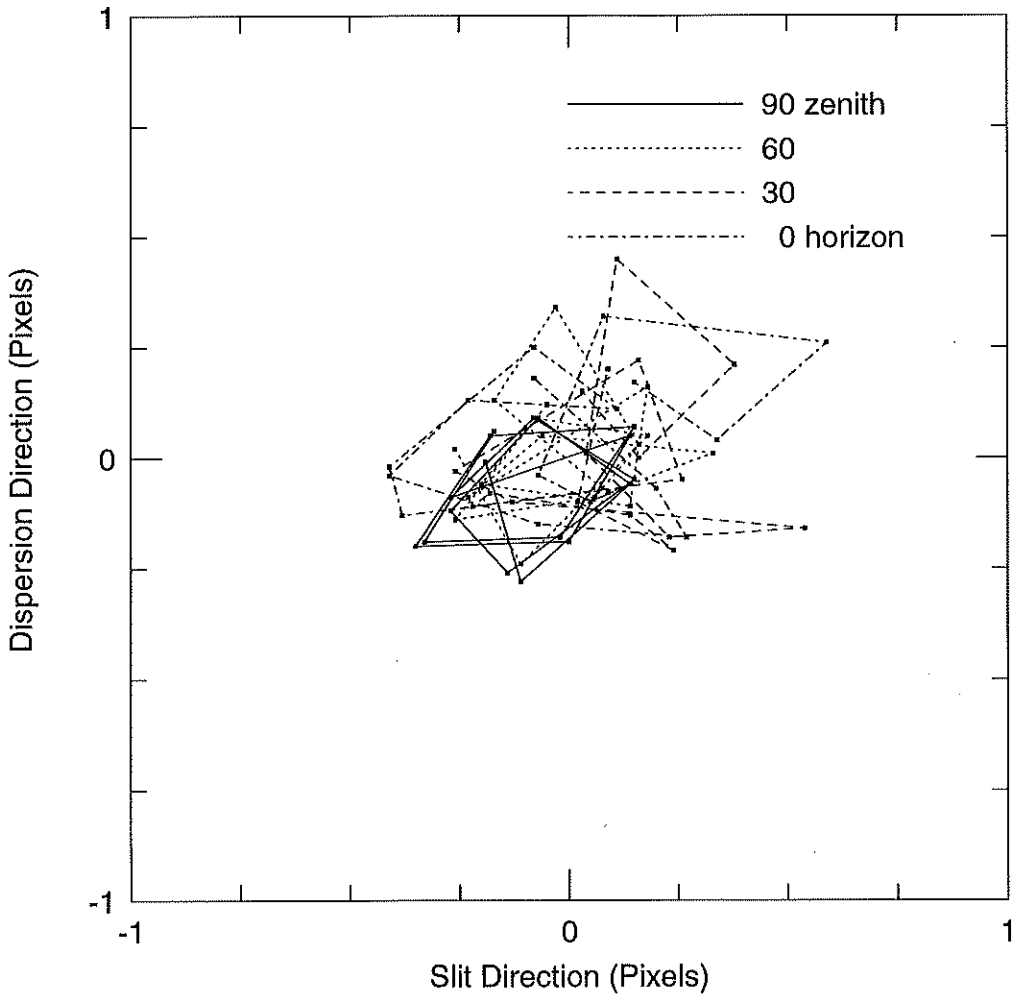

Fig. 22.— Residual errors: Echellette mode (10/1999)

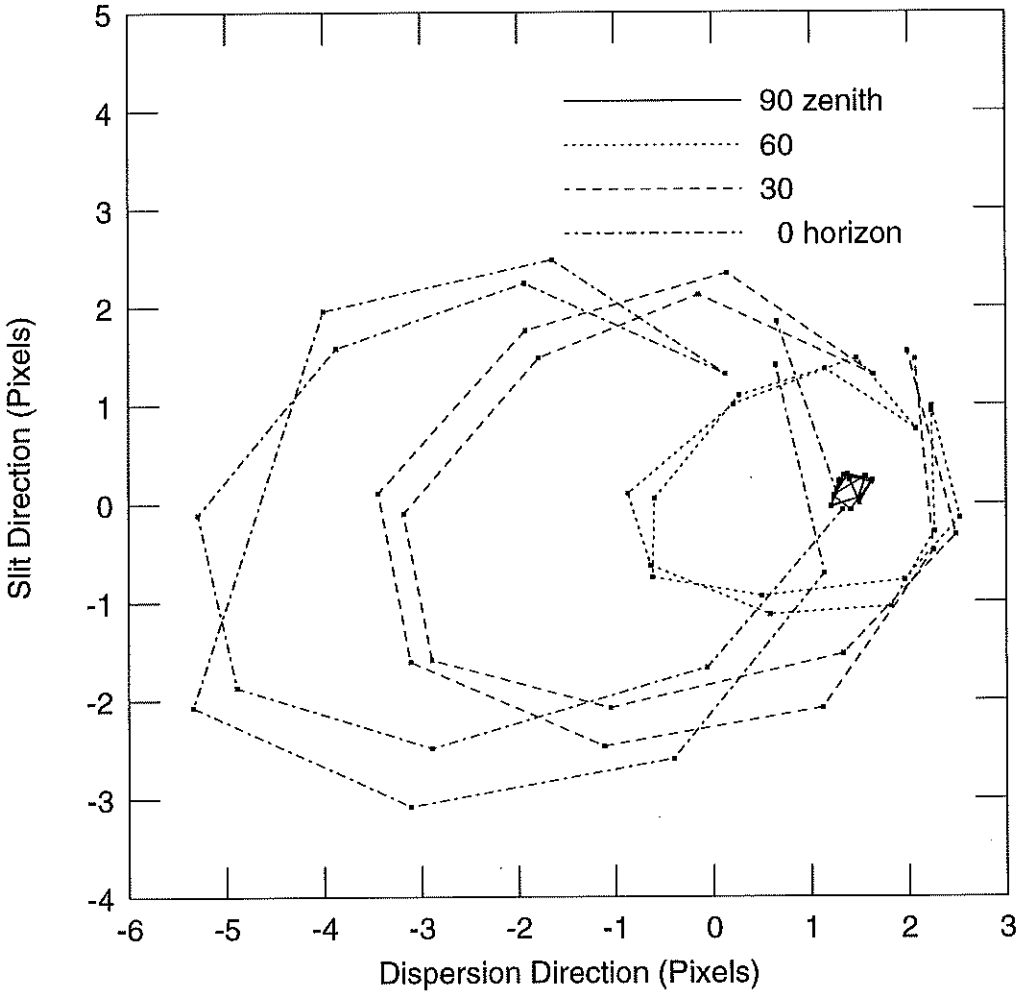

Fig. 23.— Flexure: low-resolution mode (10/1999)

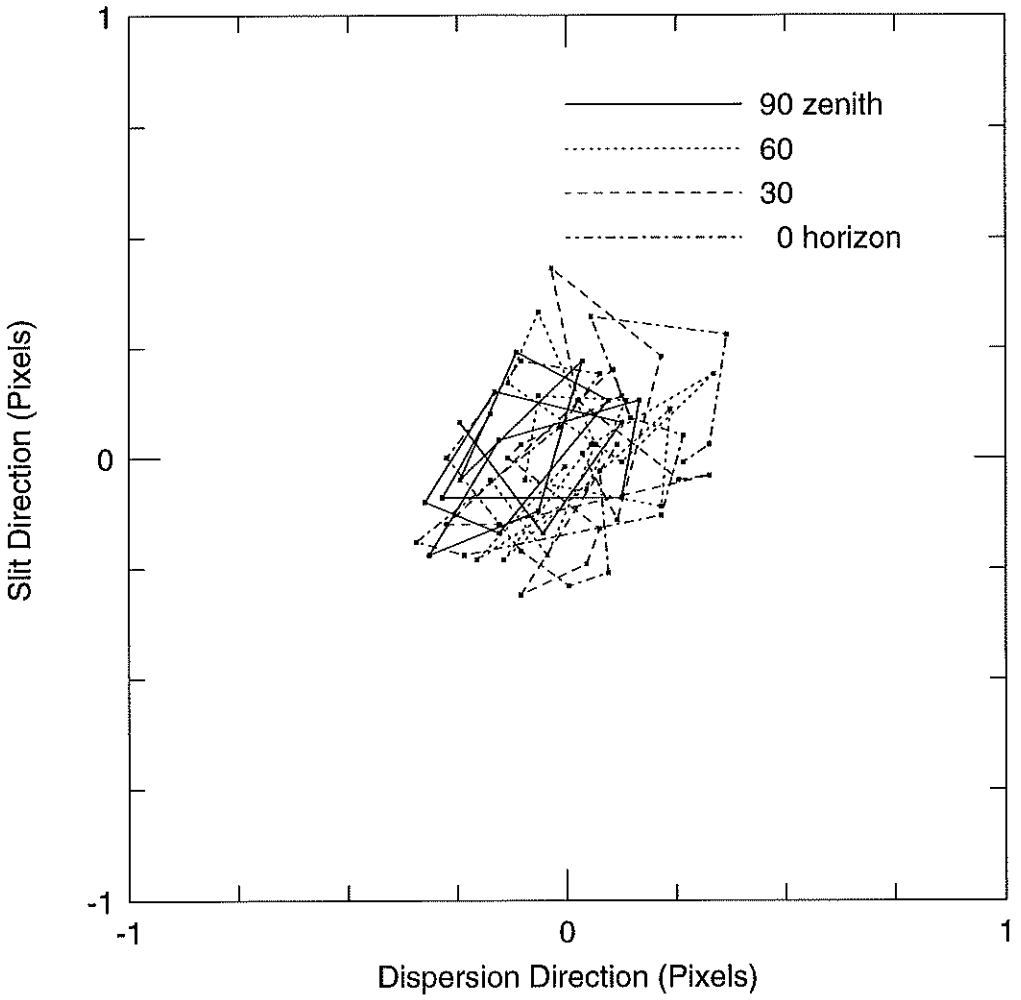

Fig. 24.— Residual errors: Low-res. mode (11/1999)

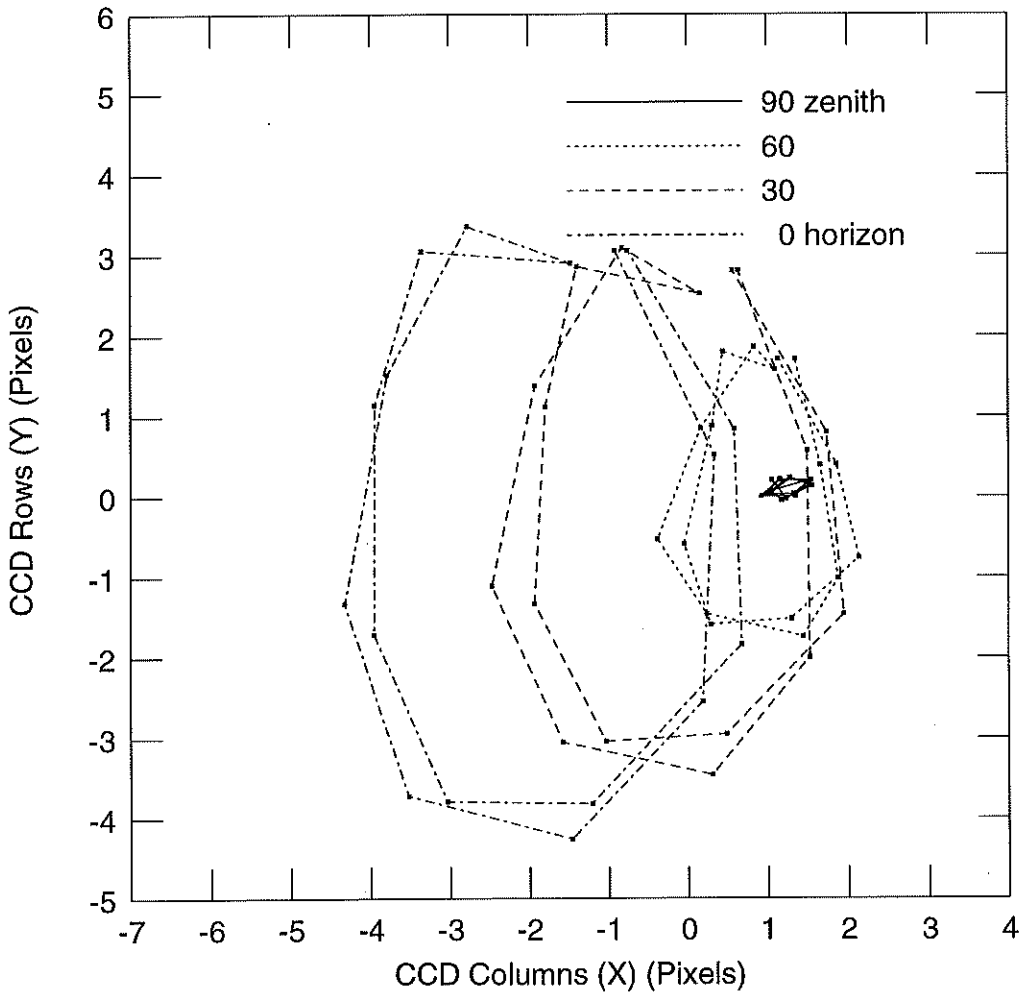

Fig. 25.— Flexure: Imaging mode (10/1999)

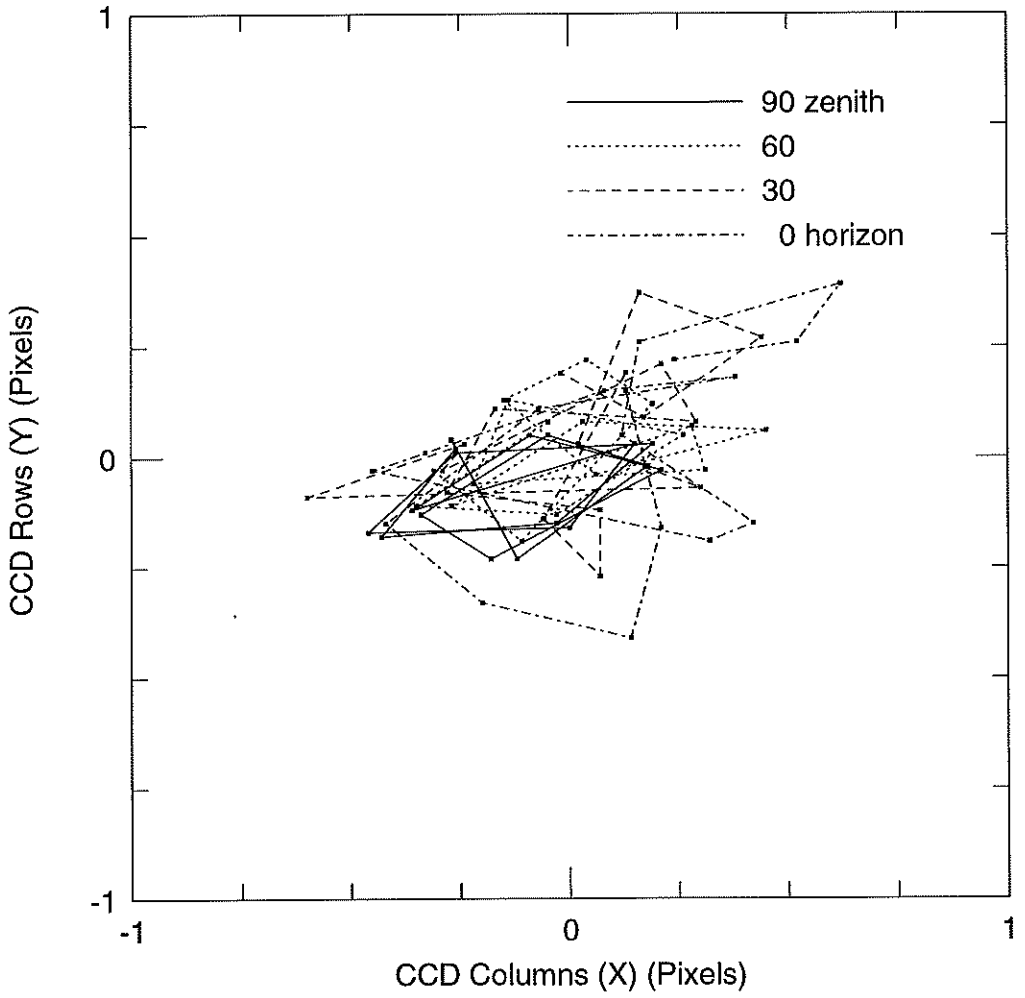

Fig. 26.— Residual errors: Imaging mode (11/1999)

orientation of the instrument relative to gravity remains constant when the instrument is rotated. There should be no gravitationally-induced flexure, and the zenith data points should appear coincident on the plot. However, these points (shown connected with solid lines) are not coincident but rather,they show a small but repeatable image motion that correlates with instrument rotation. There is out-of-roundness or runout between the instrument and the rotator module. The determinate structure that attaches ESI to the rotator module isolates most of the bearing stresses from the instrument. A small amount of residual stress contributes to the observed hysteresis and zenith motion. Image motions induced by such stresses are neither modeled nor corrected by our model of gravitationally-induced flexure.

4.2.4. Modeling

Given the space-frame structures used for esi, a linear elasticity model of gravitational flexure was used for fitting the image motion versus spectrograph position data. The equations for this gravitational flexure model are as follows:

$$X(\phi,\, \theta) = a_0 + a_1 \cos\phi \cos\theta + a_2 \cos\phi \sin\theta + a_3 \sin\phi \tag{1}$$

$$Y(\phi,\, \theta) = b_0 + b_1 \cos\phi \cos\theta + b_2 \cos\phi \sin\theta + b_3 \sin\phi \tag{2}$$

where X corresponds to the predicted position of the reference spot in the X (or column) axis of the CCD, Y the predicted position in the Y (row) axis, ϕ the telescope elevation angle, θ the rotator position angle. The parameters, a_i and b_i, $i = 0, 1, 2, 3$ are the corresponding linear coefficients obtained from a least square fit of the data to the model. Each instrument mode is fit separately.

The gravitational flexure model provides a relatively good fits to the observed data for all three modes. The worst-case residuals (vector magnitude of X and Y residuals) in

each mode were: Imaging mode, 0.63 pixels; Low-resolution mode, 0.66 pixels; Echellette mode, 0.64 pixels. The corresponding RMS residual errors were: Imaging mode, 0.29 pixels; Low-resolution mode, 0.25 pixels; Echellette mode, 0.25 pixels. These residuals are not unreasonable given the non-modeled image motions observed at zenith plus the several tenths of a pixel hysteresis observed at all positions. Since one pixel corresponds to 0.″153 on the sky, worst-case residuals were about 0.″1 and RMS residuals were about 0.″04.

Mechanical hysteresis is significant and comparable to flexure residuals, especially when the telescope is operating at lower elevations. Fig. 27 plots the absolute value of the difference between the coordinates of the echellette mode central reference feature as observed on pairs of observations obtained at the same elevation and rotator position angles but arrived at from opposite directions of rotator motion. It is clear that hysteresis increases significantly with increasing elevation angle. The mechanical sources for this hysteresis should be investigated, and if possible, reduced.

4.2.5. Operational Performance

To validate the gravitational flexure model and the overall operation of the FCS, the sequence of images described in Section 4.2.3 was repeated for each mode, except this time the FCS system was turned on. The results of these measurements are shown for all three instrument modes as Figs. ??, ??, and ??. These represent worst-case errors over the entire sky. For a typical exposure, residual errors would be a few tenths of a pixel, or about 0.″04 on the sky. By comparing these to the corresponding measurements obtained with the FCS turned off (see Figs. 21, 23, and 25), it is clear that the FCS has significantly reduced flexure-induced image motion in all three modes.

The measurements depicted in Figs. ??, ?? and ?? only demonstrate how well the

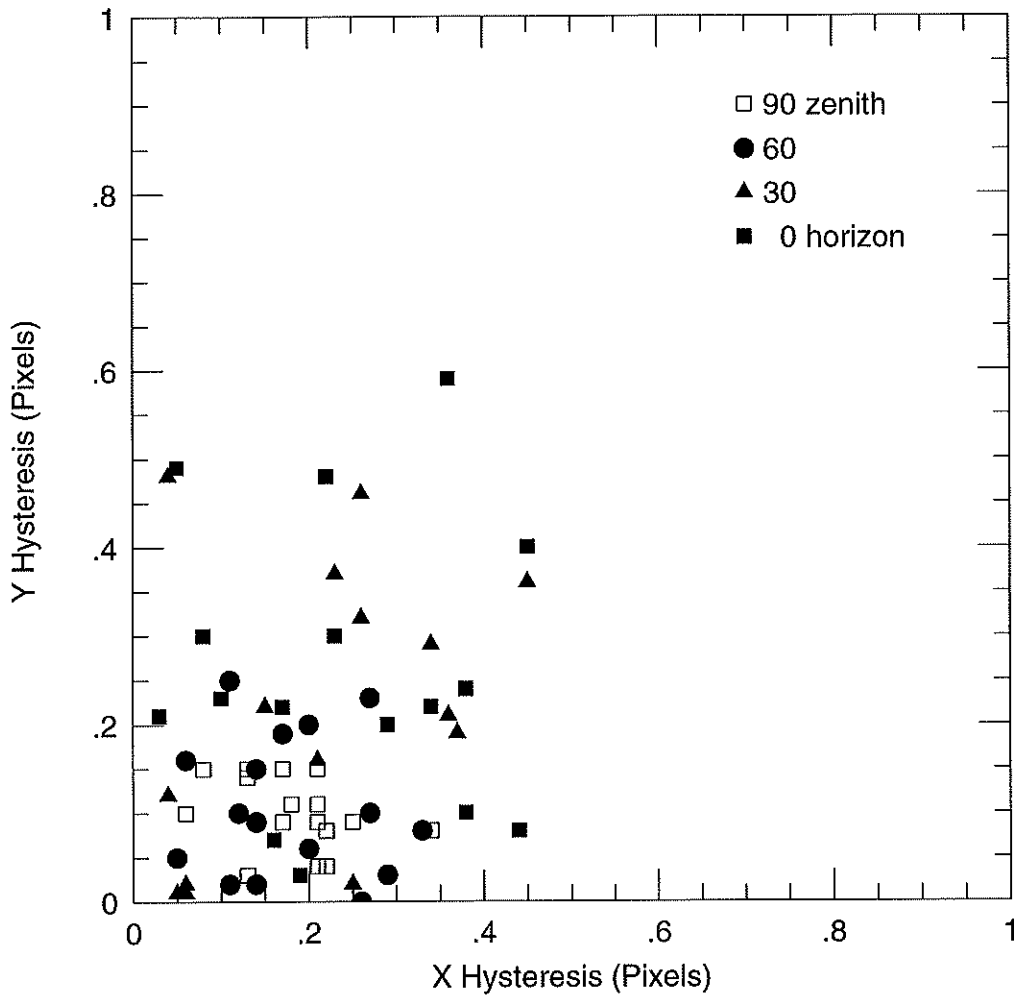

Fig. 27.— Flexure: Imaging mode (10/1999)Hysteresis of paired points

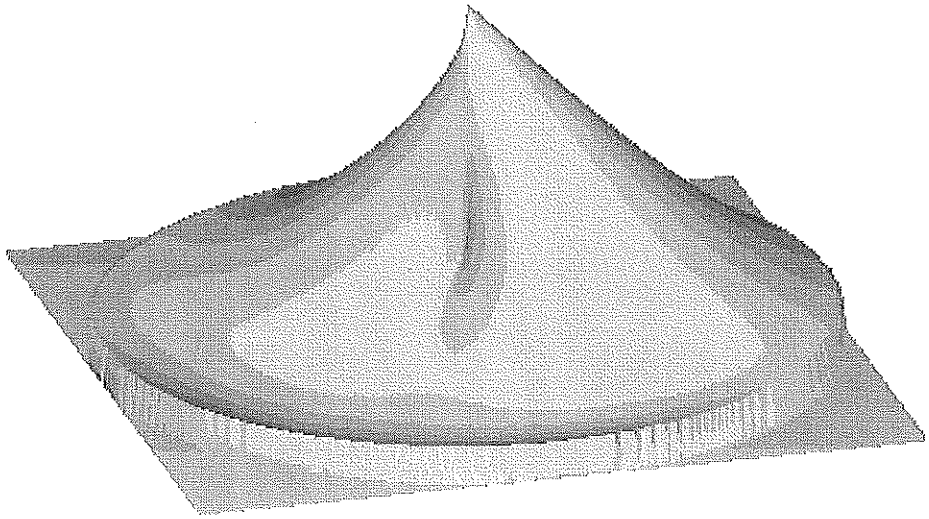

Fig. 28.— X component of echellette flexure model

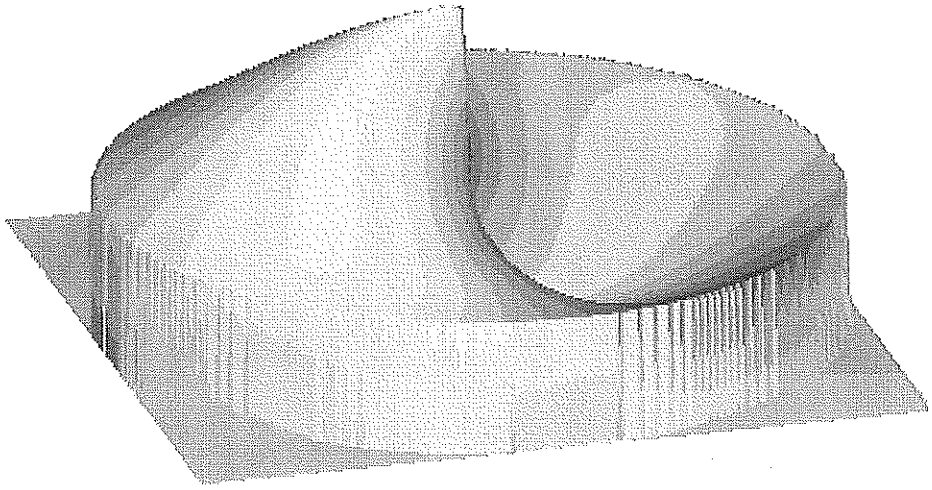

Fig. 29.— Y component of echellette flexure model

single, central reference feature was stabilized for each instrument mode. To confirm whether stabilizing this feature was sufficient to stabilize the image across the entire CCD, a more extensive analysis of the echellette mode FCS calibration data was performed Kibrick et al. (2000b). That analysis found no significant field rotations, and only slight scale changes on the order of a few tenths of a pixel across the length and width of the detector. Thus, the entire image was stabilized. With the FCS system turned on, both image motion and the scale change in the slit direction were significantly reduced, while scale change in the dispersion direction was unchanged.

4.2.6. Long Term Results

The long-term stability of the FCS calibration has been measured by comparing the echellette mode flexure models that were derived from flexure calibrations performed in October and November 1999 with those obtained from a pair of calibrations conducted on the same night in March 2001. While some large zero-point shifts (the a_0 and b_0 terms) were observed when comparing the 2001 calibrations to those performed in 1999 (see Table 8), these were most likely the result of an adjustment to the Dewar position performed in January 2000. However, the zero point stability over the course of one night is about 0.15 pixel. Thus, one can compensate for any longer-term zero point shifts by taking a single calibration exposure at the start of the night and adjusting the FCS operational zero-point accordingly.

While the values of the remaining model coefficients (a_1, a_2, a_3, and b_1, b_2, b_3) varied by as much as 20% from one calibration model to the next, the models they represent agree quite closely, once the respective zero-points are aligned. The X and Y components of a flexure model (with the a_0 and b_0 terms set to zero) can each be visualized as a 3D surface. For example, see Figs. 28 and 29 which illustrate the X and Y components of the

echellette-mode flexure. In these Figures, the azimuthal axis corresponds to θ, the radial axis to zenith distance, or $90 - \phi$, and the Z axis to the predicted flexure, which in these two examples varies between 0 and 6 pixels. Each of the four models was used to generate a pair of surfaces using a uniform grid with grid points spaced one degree apart in both the θ and ϕ axes. Pair-wise comparisons between the corresponding surfaces representing each of the four models were performed for all possible model pairings. The worst-case differences observed between corresponding points in any of these pairings was 0.43 pixel in X and 0.24 pixel in Y. The RMS errors across all four models were 0.11 pixels in X and 0.07 pixels in Y.

Based on these results, and assuming that no significant mechanical or optical modifications are made to the instrument, a given flexure calibration model can be expected to provide acceptable FCS performance for at least one year. Thus, aside from nightly checks of the FCS zero point, frequent recalibration of the flexure model is not needed to maintain FCS performance.

5. Optical Performance

In the following section we report on the optical and mechanical performance of the spectrograph. The theoretical performance is based on interfacing a detailed optical model with a mechanical model. The measured performance is based on the results of a comprehensive testing program at the Lick Observatory Instrument Laboratory prior to shipping the instrument and a complimentary set of tests performed in the telescope. We now detail much of the modelling and testing along with the performance report.

Table 8: Echellette mode model terms and statistics

TERM	October 1999	November 1999	March 2001 #1	March 2001 #2
a_0	1397.24	1382.72	1328.05	1327.90
a_1	1.498 ± 0.049	1.577 ± 0.054	1.663 ± 0.076	1.588 ± 0.078
a_2	1.544 ± 0.051	1.632 ± 0.051	1.576 ± 0.069	1.537 ± 0.070
a_3	3.278 ± 0.064	3.074 ± 0.068	3.345 ± 0.092	3.496 ± 0.095
σ_x	0.20 pixels	0.21 pixels	0.20 pixels	0.21 pixels
b_0	2023.98	2024.08	2027.13	2027.25
b_1	-2.088 ± 0.037	-2.024 ± 0.037	-2.027 ± 0.052	-1.884 ± 0.102
b_2	0.561 ± 0.039	0.583 ± 0.035	0.542 ± 0.047	0.636 ± 0.092
b_3	0.316 ± 0.049	0.503 ± 0.047	0.481 ± 0.063	0.314 ± 0.124
σ_y	0.15 pixels	0.15 pixels	0.14 pixels	0.27 pixels

5.1. Direct-Imaging and Spectral-Imaging Performance

5.1.1. Predicted System Performance

The theoretical end-to-end system performance is described in this section. A system analysis for the pre-contsruction design was calculated with an in-house lens analysis code written by one of the authors (B.S.).

The system performance reported here was calculated using the final as-built camera. Orders 6 in the infra-red through 15 in the blue were ray traced at five wavelengths uniformly spaced over each free-spectral range without refocus. The rms spot-size diameter, D_{rms} was calculated for each image. Averaging these image diameters over all wavelengths and all orders the Ave(rms) = 19.0 +/- 3.3 microns. The corresponding 80% encircled ray diameter average is Ave(80%) = 22.5 +/- 4.2 microns, while Ave(90%) = 28.4 +/- 5.6 microns. RMS spot diameters at the center of each order are shown for all orders in Table 9. Table 1 shows the predicted RMS spot diameters for several field points with no imaging filter in place, i.e., the full (0.39 to 1.10)-micron wavelength range without refocus.

5.1.2. Measured System Performance

We now describe the optical performance tests which were done during instrument commissioning.

After assembly and integration into the Keck II telescope, a series of optical tests was performed to assess the optical performance of the instrument. In the imaging mode, optical performance was analyzed by imaging an array of pinholes placed in the slit mask location. In the LDP mode a linear array of pinholes was used and in the echellette mode a single pinhole was used. The pinholes are 125 microns in diameter, which projects to 16.8

microns at the detector apart from anamorphics factors (compared to 15 micron pixels). Thus they contribute slightly to measured spot sizes. The pinholes were illuminated by either the dome floodlamps or by the internal quartz-halogen flat lamp. The case of dome illumination most accurately mimics the star illumination as the Keck II pupil is imaged into esi. In the case of internal flat-field lamps, internal baffles become the system stop. These apertures are larger than the Keck pupil and not hexagonal. Thus the artificial source tests overestimate the image sizes due to overfilling of the camera pupil. For the case of imaging mode the standard filter set provided with ESI (Johnson B & V, Spinrad R and Gunn I) and no-filter were used. In all cases, a series of images was taken at a range of focus settings.

Image quality was determined by fitting each spot to a two-dimensional azimuthally-averaged Gaussian distribution using Information Data Language (IDL), (Research Systems Boulder, CO). The radial profiling routine returns the standard deviation for each fitted Gaussian. These were converted to the two dimensional RMS spot diameters (D_{rms}) by multiplying the standard deviation by 2.828. D_{rms} was determined for a variety of wavelengths as a function of focal position in the two spectroscopic modes. In the imaging mode D_{rms} was determined for a variety of field positions as a function of focal position. These data are plotted in Figure 32. The D_{rms} values in this plot were computed as the median over location on the chip of the D_{rms} values as a function of camera focal position.

The D_{rms} at best focus is compared to that predicted for the design in Table 9. The data in Table 9 shows a discrepancy between design prediction and measured D_{rms}. This discrepancy is due in part to fabrication and assembly errors, but is probably due mostly to the improper illumination in the testing, as mentioned above. This assertion is based on the results of the globular cluster tests below and the initial camera testing, which imply better performance than this artificial star test.

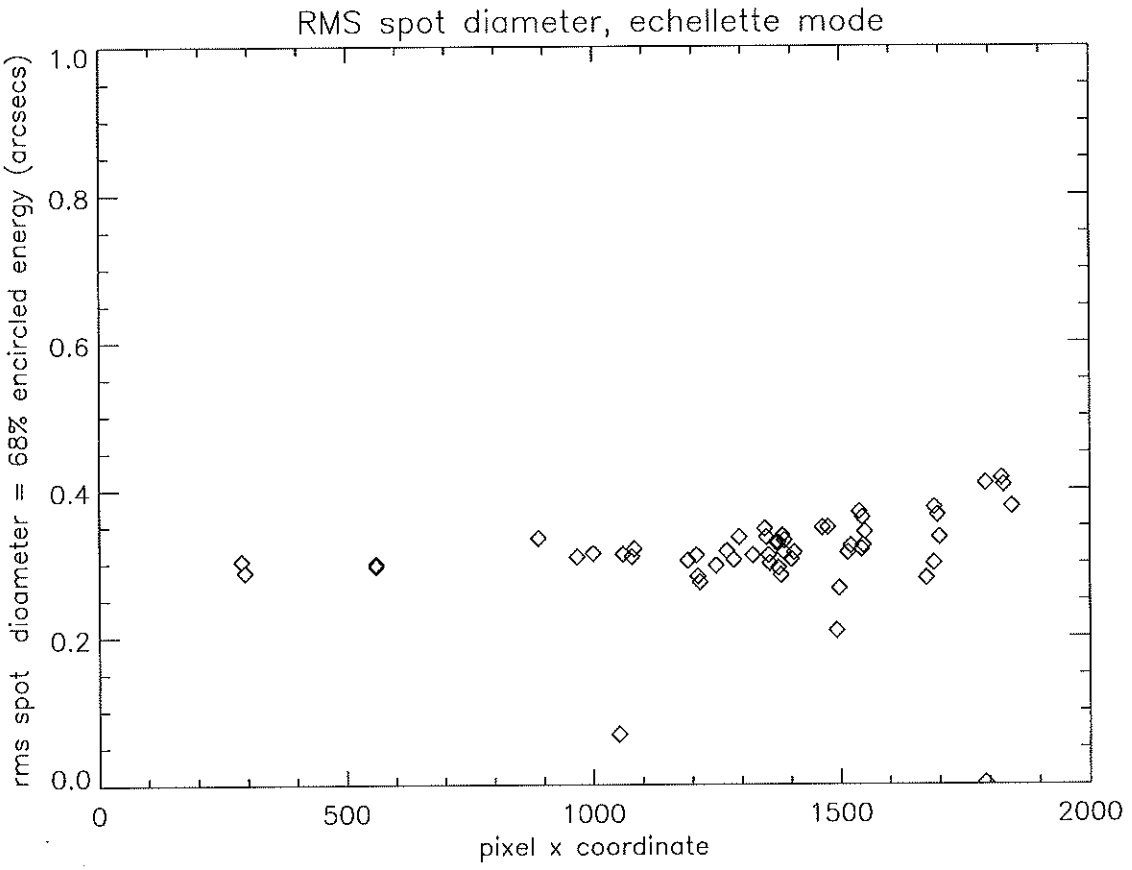

Fig. 30.— **R**MS spot diameters, echellette mode.

Table 9: Median rms spot diameters

	measured		design	
Mode	μ	arcseconds	μ	arcseconds
Echellette	31.7	0.32	19	0.19
LDP	30.8	0.31	16	0.16
Imaging	37.4	0.38	24	0.25

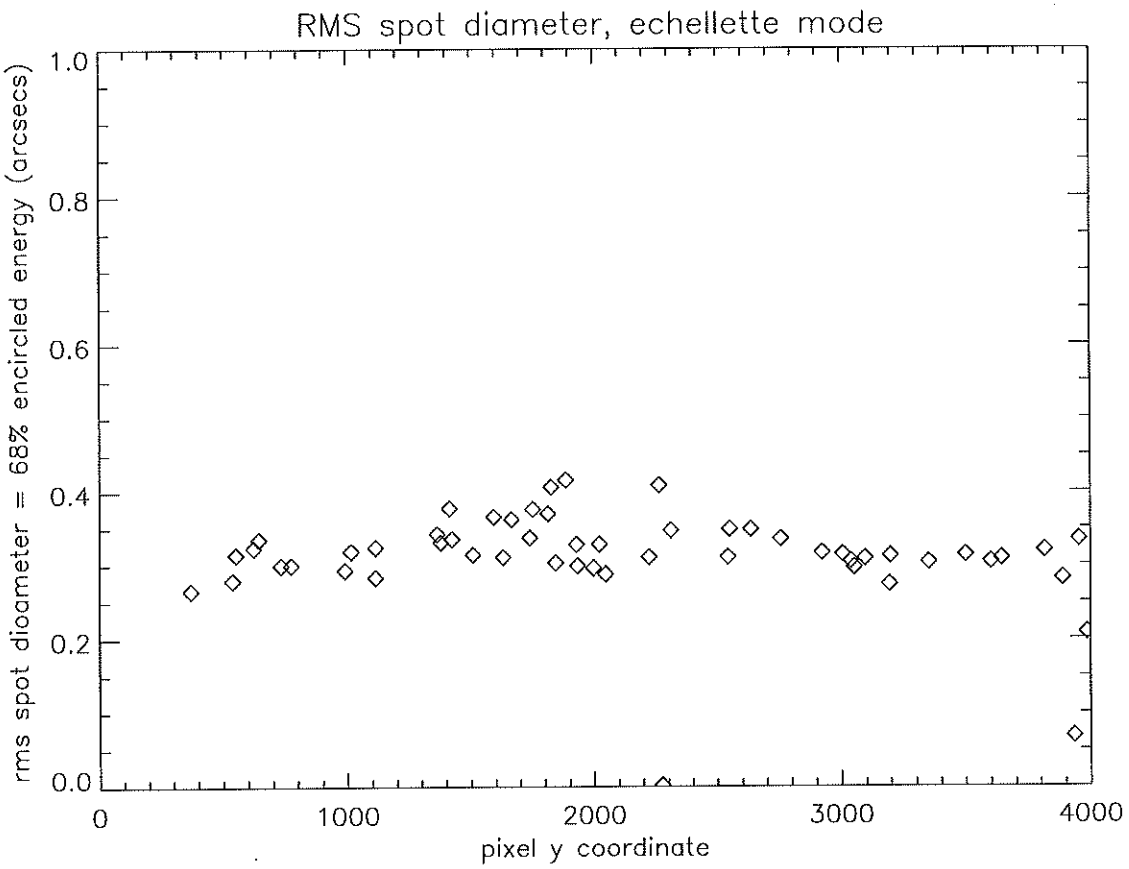

Fig. 31.— RMS spot diameters, echellette mode.

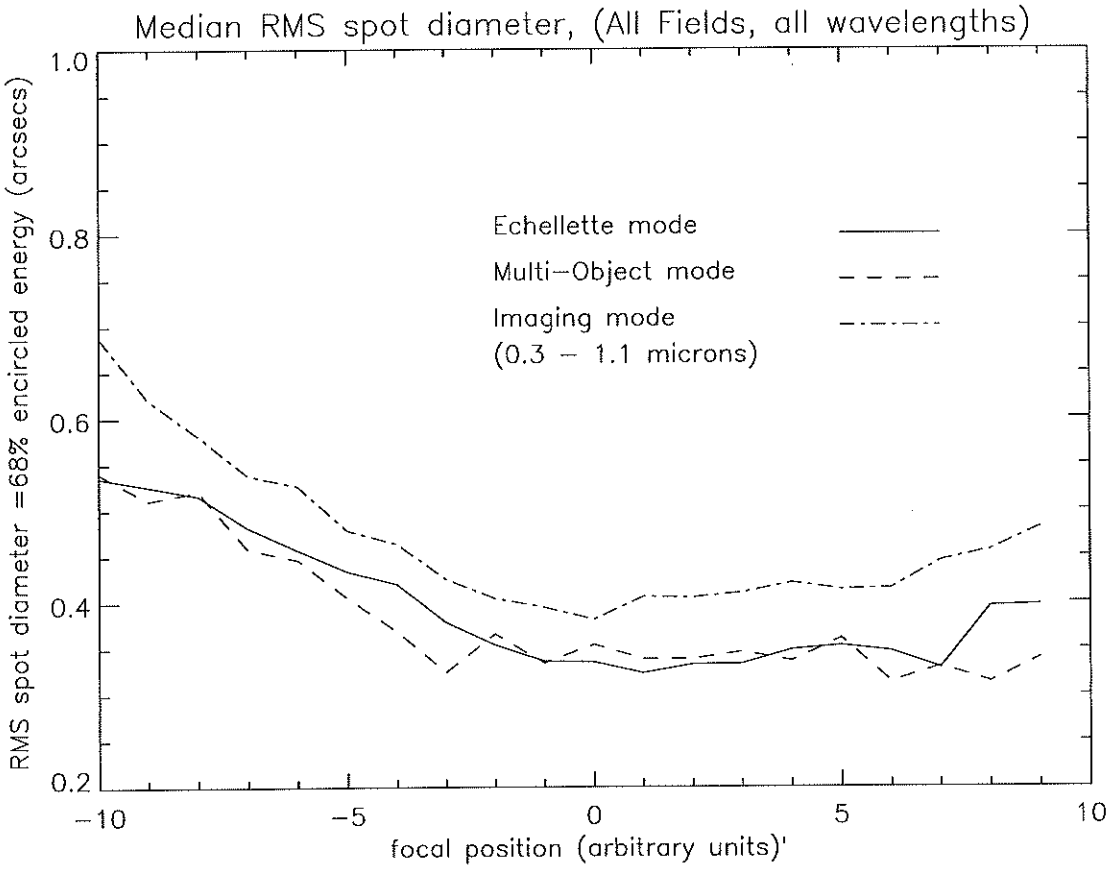

Fig. 32.— **R**MS spot diameters, echellette mode, through focus.

Figure 30 and Figure 31 show D_{rms} as a function of position on the chip for the echellette mode. The uniformity of the spot size as a function of location is an indication that the field curvature and chip tilt are negligible

Several globular clusters were observed in BVRI, under good seeing conditions. The FWHM was calculated for each image using the IRAF image reduction package. This was done by fitting the azimuthally averaged images to Gaussian energy distributions. The quality of the fit and the FWHM of the fitted images are displayed in Figure 33 and Figure 34.

The average I band images show a FWHM of 0.″34 . This is consistent with the best FWHM seeing disk of 0.″25 convolved with an average instrumental FWHM of 0.″27 assuming no guiding errors. These are the best non-AO optical images at Keck to date.

5.2. Efficiency

5.3. Instrument Efficiency in Echellette Mode

Observations of the spectrophotometric standard Wolf 1348 were made through a 6"-wide slit during the September 1999 commissioning run. The observations were corrected for an airmass of 1.04 using the mean extinction curve for Mauna Kea downloaded from the Canada-France-Hawaii WWW site. The values for flux/wavelength for Wolf 1348 were taken from the tables Massey et al. (1988), Massey & Gronwall (1990) and converted into photons per second per angstrom using the relation:

$$N_\lambda = \frac{4.275X10^{12}}{\lambda} 10^{\frac{-(m_\lambda + A_\lambda X)}{2.5}}$$

Here m_λ is the magnitude from the Massey et al. (1988) tables, A_λ is the extinction in magnitudes per airmass at λ and X is the airmass of the observation.

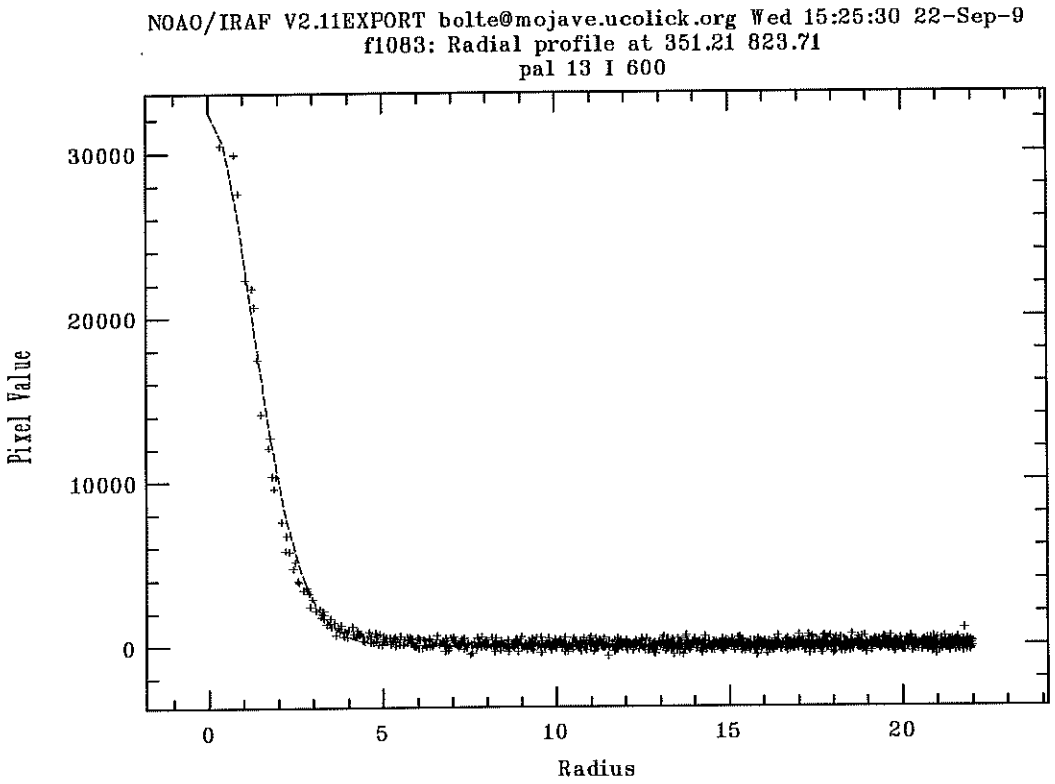

Fig. 33.— FWHM I band inage of Palomar 13.

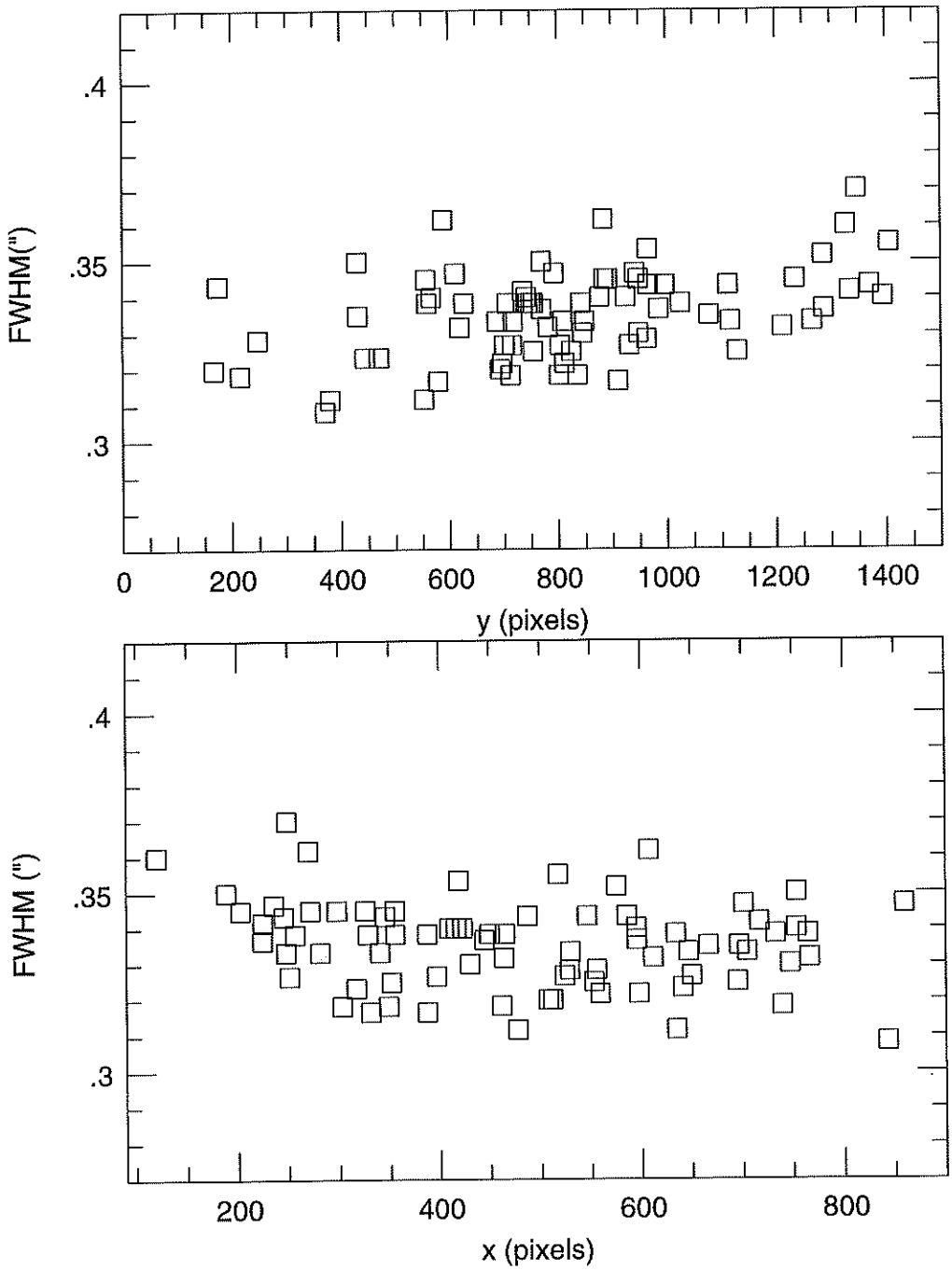

Fig. 34.— FWHM I band inage of Palomar 13 .

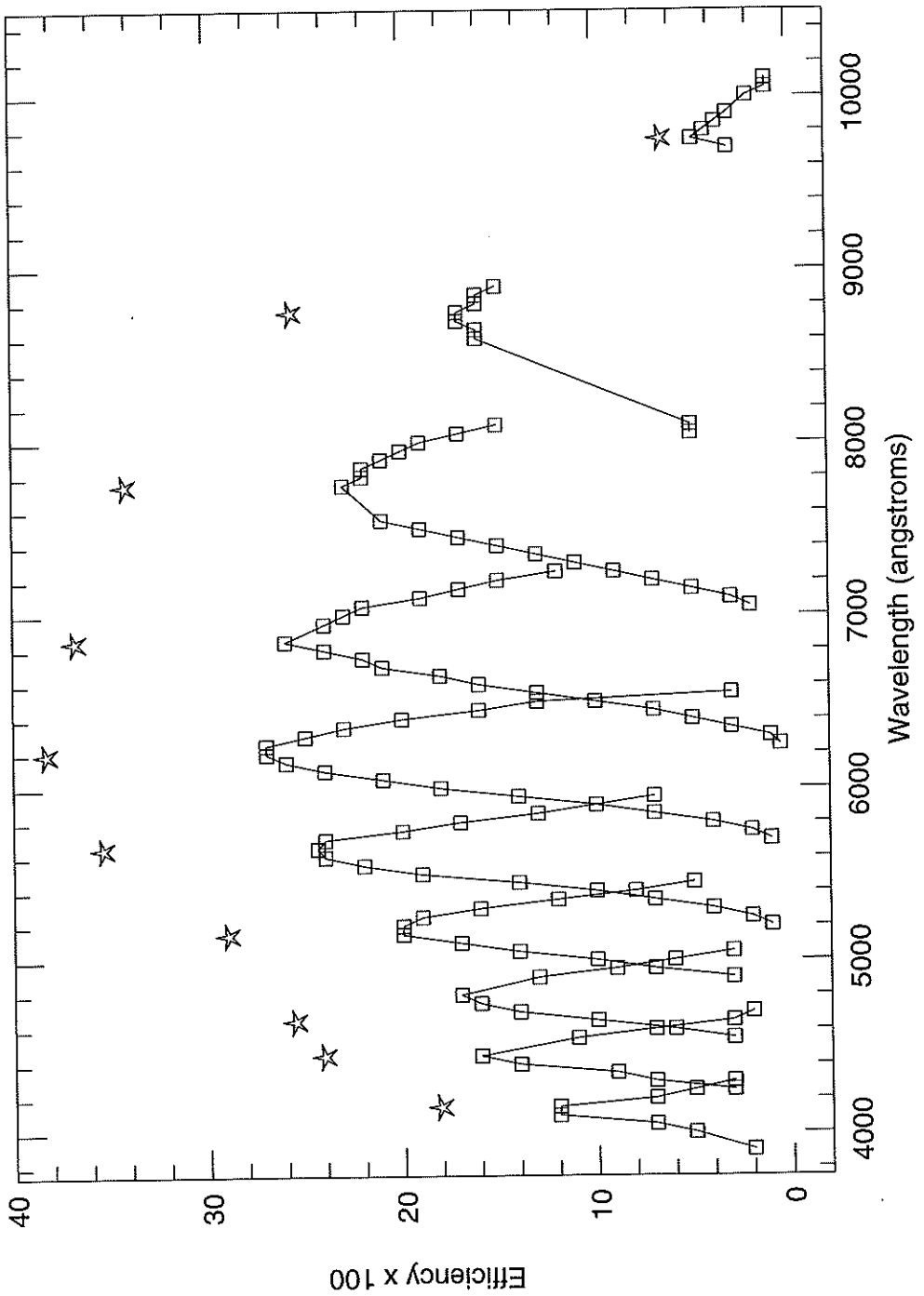

Fig. 35.— Instrument efficency in echellette mode.

Figure 35shows the the ratio of the number of photons predicted for Wolf 1348 to the number detected (corrected to the top of the atmosphere). The solid line connecting open squares is the measured efficiency for each order after removing the effects of atmospheric extinction. The five-point stars show the total *instrument* efficiency at the peak of each order after backing out the effects of two reflections off aluminum surfaces. The aluminum efficiency curve for the secondary assumed 'fresh' aluminum, this was reduced by 5% for the primary which was known to have been degraded by at least this amount at the time of the observation. The plot show efficiency calculated order by order (that is, not summing the flux at a given wavelength that is detected in more than one order). For the bluer orders, adding flux from adjacent orders at common wavelengths increases the overall throughput at some wavelengths by as much as 60%.

5.4. Instrument Efficiency in LDP Mode:

Figure 36shows the the ratio of the number of photons predicted for Wolf 1348 to the number detected (corrected to the top of the atmosphere). The solid line is the measured efficiency after removing the effects of atmospheric extinction.

The efficiency in LDP mode has been measuerd to be at least 10% better than in the echelle mode. The greater efficency in LDP mode is due primarily to the greater reflectivity of the LDP fold mirror over the grating. The beam in LDP mode shares a common path with the echelle mode except for this fold mirror, which relaces the grating in LDP mode.

6. Conclusion and Acknowledgments

We have discussed the design, the engineering development, the construction and the implementation of the ESI spectrograph. We have given an overview of all of the major

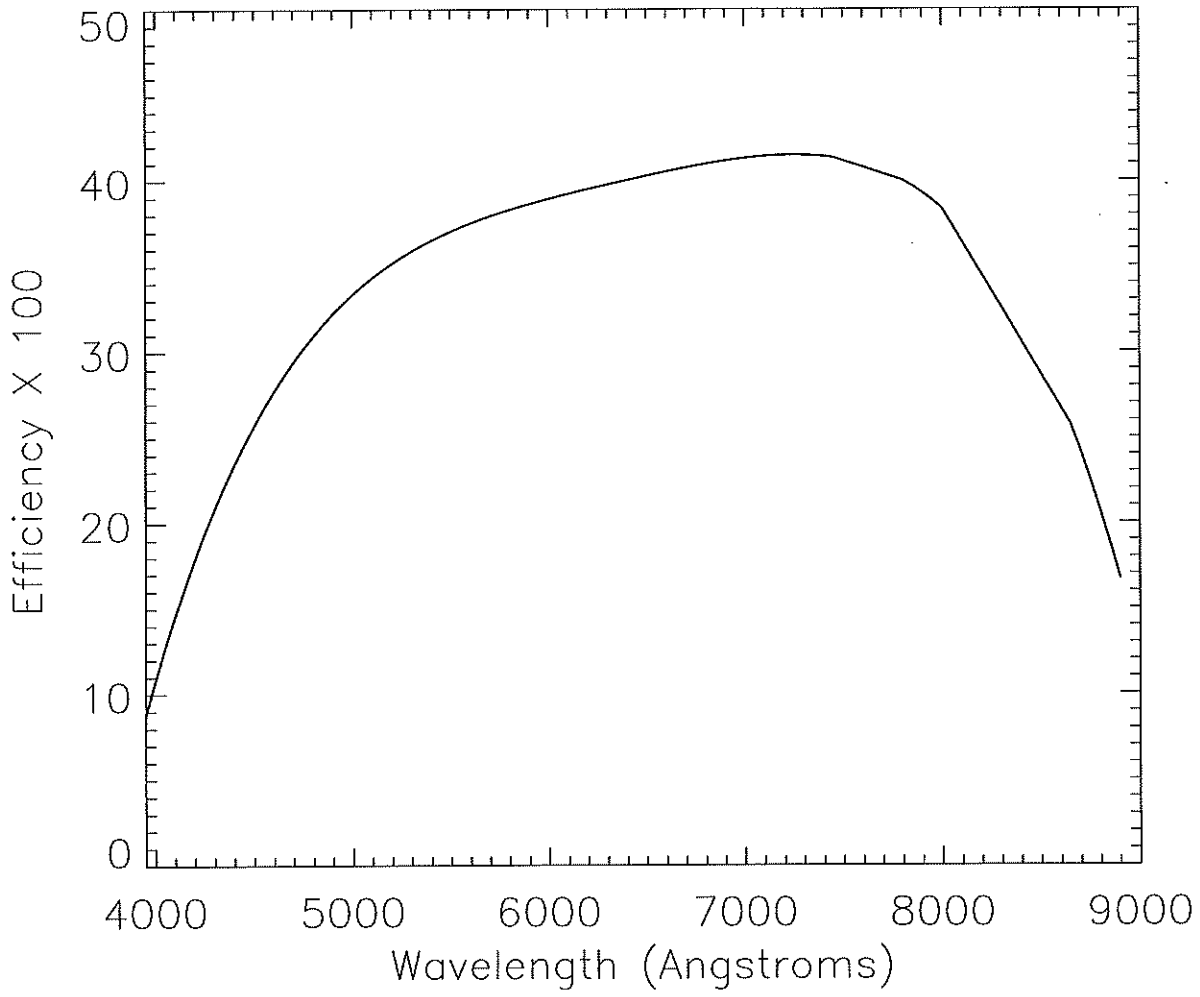

Fig. 36.— Instrument+telescope efficency in prismatic mode.

subsystems together with the most important of the design criteria. Performance has been analysed in terms of throughput, image diameters, and residual flexure. Imaging studies of globular clusters have produced the best visible images to date at Keck Observatory. Throughput of the telescope and the instrument (including the CCD detector) in echellette mode has been observed to be as high as 28%in echellette mode and has been observed to be as high as 40% in LDP mode.

The authors wish to thank the entire technical staff at Lick Observatory, including (in no particular order): in the Electronics laboratory : Barry Alcott, Ted Cantrall, Carol Harper and Jim Burrous (deceased); in the Instrument Laboratory: Jeff Lewis, Dick Kanto, Terry Pfister, Jim Ward and Gary Dorst; in the Optical Laboratory: David Hilyard; in the Engineering department: David Cowley, Carol Osborne, Jack Osborne, Vern Wallace, Chris Wright, Mary Poteete and Heather Mietz; in the Software development department: De Clark, Steve Allen and Dean Tucker; in the detector development laboratory: Richard Stover, Mingzhi Wei, Kirk Gilmore, Bill Brown, and Lloyd Robinson and in the business office: Maureen McLean, Marlene Couture and Edna Sandberg.

The authors also wish to thank Jerry Nelson and Terry Mast for their many insightful comments and suggestions. We would especially like to thank Bob Goodrich and the staff at Keck Observatory for their help with the assembly, testing and data acquisition for this instrument.

REFERENCES

Bigelow, B. C. & Nelson, J. E.: 1998, *Proc. SPIE* **3355**, 164

Epps, H. W.: 1998, *Proc. SPIE* **3355**, 111

Epps, H. W. & Miller, J. S.: 1998, *Proc. SPIE* **3355**, 48

Hilyard, D. F., Laopodis, G. K., & Faber, S. M.: 1999, *Proc. SPIE* **3786**, 482

Iraninejad, B., Lunliner, J., Mast, T., & J., N.: 1987, *"Keck Observatory Technical Report"* 160

Kibrick, R. I., Miller, J. S., Nelson, J. E., Radovan, M. V., Sheinis, A. I., & Sutin, B. M.: 2000a, *Proc. SPIE* **4009**, 262

Kibrick, R. I., Miller, J. S., Nelson, J. E., Radovan, M. V., Sheinis, A. I., & Sutin, B. M.: 2000b, in *Proc. SPIE Vol. 4009, p. 262-273, Advanced Telescope and Instrumentation Control Software, Hilton Lewis; Ed.*, Vol. 4009, pp 262–273

Leach, R. W., Beale, F. L., & Eriksen, J. E.: 1998, *Proc. SPIE* **3355**, 512

Massey, P. & Gronwall, C.: 1990, *ApJ* **358**, 344

Massey, P., Strobel, K., Barnes, J. V., & Anderson, E.: 1988, *ApJ* **328**, 315

Nelson, J. R., Lubliner, J., & Mast, T. S.: 1982, *Proc. SPIE* **332**, 212+

Oke, J. B., Cohen, J. G., Carr, M., Dingizian, A., Harris, F. H., Lucinio, R., Labrecque, S., Schaal, W., & Southard, S.: 1994, *Proc. SPIE* **2198**, 178

Prochaska, J. X., Gawiser, E., & Wolfe, A. M.: 2001, *ApJ* **552**, 99

Radovan, M. V., Bigelow, B. C., Nelson, J. E., & Sheinis, A. I.: 1998, *Proc. SPIE* **3355**, 155

Sheinis, A. I., Nelson, J. E., James, E. C., & Radovan, M. V.: 1999a, *Proc. SPIE* **3786**, 350

Sheinis, A. I., Nelson, J. E., & Radovan, M. V.: 1998, *Proc. SPIE* **3355**, 59

Sheinis, A. I., S., M. J., Bolte, M., & Sutin, B. M.: 2000, *Proc. SPIE* 4008

Sheinis, A. I., Sutin, B. M., Epps, H. W., Schier, J. A., Hilyard, D. F., & Lewis, J.: 1999b, *Proc. SPIE* **3786**, 413

Sutin, B. M.: 1997, *Proc. SPIE* **2871**, 1116